Eur. J. Mineral.
2015, **27**, 31–50
Published online 21 October 2014

**Dedicated to the memory of**
**Enzo M. Piccirillo**

# Magnetite from the Cogne serpentinites (Piemonte ophiolite nappe, Italy). Insights into seafloor fluid–rock interaction

SUSANNA CARBONIN[1,*], SILVANA MARTIN[1], SIMONE TUMIATI[2] and PIERGIORGIO ROSSETTI[3]

[1] Dipartimento di Geoscienze, Università di Padova, via Gradenigo 6, 35100 Padova, Italy
*Corresponding author, e-mail: susi.carbo@hotmail.co.uk
[2] Dipartimento di Scienze della Terra, Università di Milano, via Mangiagalli 34, 20133 Milano, Italy
[3] Dipartimento di Scienze della Terra, Università di Torino, via Valperga Caluso 35, 10125 Torino, Italy

**Abstract:** In the Cogne area (Aosta Valley, Western Italian Alps), magnetite mineralization occurs associated with different types of serpentinite (pseudomorphic, rodingitic and magnetite-rich serpentinites), which are also heterogeneous in terms of bulk chemical composition, mineral assemblage and mineral chemistry.

The mineralization is hosted by a lizardite-, ±chrysotile-bearing serpentinite showing a pseudomorphic texture after oceanic peridotite. It contains fine-grained magnetite showing oscillatory zoning with Cr-poor cores (~ 0.4 wt.% $Cr_2O_3$), which are surrounded by Cr-rich inner euhedral rims (up to 17.0 wt.% $Cr_2O_3$), mantled in turn by partially resorbed Cr-bearing outer rims (~ 2.0 wt.% $Cr_2O_3$). This dramatic variation of Cr content in magnetite is described by the exchange vector $Fe^{3+}$ $Fe^{2+}$ $Cr^{3+}_{-1}$ (Mn, Zn, Ni) $^{2+}_{-1}$. The absence of Cr-rich spinel cores suggests that the source of chromium was the Cr-Tschermak component of the orthopyroxene, made available during the serpentinization-related breakdown. In these rocks, lizardite, the primary serpentine phase, is partially overgrown by prograde antigorite, indicating that serpentinization occurred under relatively low-*T* conditions in a pre-orogenic (*i.e.*, oceanic) setting, and was followed by an Alpine metamorphic re-equilibration.

Rodingitic serpentinite and serpentinite rich in magnetite are composed of, in highly variable amounts, diopside (locally with inclusions of partially disordered graphite), calcite, magnetite, andradite/hydroandradite, prograde olivine, brucite and serpentine (mostly antigorite but also relict lizardite), with minor chlorite and accessory apatite. Magnetite content can be very high. In these rocks, magnetite is exceptionally Cr-poor (almost Cr-free). Such almost Cr-free magnetite is characterized by significant $Fe^{2+} \leftrightarrow Mg$ substitution (2–15 mol.% $MgFe_2O_4$). Crystal-chemical investigations confirm that Mg, as in magnesioferrite, shows a strong preference for the octahedral site. Due to $Fe^{2+} \leftrightarrow Mg$ substitution, the $Fe^{2+}$ content available for $Fe^{2+} - Fe^{3+}$ electron hopping in the octahedral site decreases leaving $Fe^{3+}$ in excess and giving rise to a charge increase. Additionally, a small $Fe^{3+}$ - $Fe^{2+}$ disorder is present at the tetrahedral site ($Fe^{2+}T = 0.07$ apfu).

The bulk-rock compositions and the mineral associations of rodingitic serpentinite and serpentinite rich in magnetite point to a strong metasomatism and iron mobilization sustained by $CO_2$-bearing fluids, developed at the expense of the host serpentinite. These processes likely occurred on the Tethyian seafloor, mediated by fluids sourcing from hydrothermal vents.

Thermodynamic modelling suggests that mineral assemblages observed in the Cogne area are consistent with a process of serpentinization coupled with Ca (±Al) metasomatism at 300–360°C. This might have been driven by carbon-saturated C-O-H fluids characterized by $CO_2$ contents comparable to present-day seawater, capable of fixing the redox potential of rocks close to the fayalite–magnetite–quartz buffer. Nevertheless, magnetite and associated Fe-Ni sulphides suggest slight variations in $fO_2$ (and $fS_2$) conditions recorded, ranging from relatively reducing (magnetite–heazlewoodite–pentlandite ± pyrrhotite) towards rather oxidizing (magnetite–millerite–pyrite) assemblages.

**Key-words:** Cogne; magnetite; hydrothermalism; structure refinement; serpentine minerals; micro-Raman; COH fluids.

## Introduction

Magnetite of the Cogne ore deposit, associated with the serpentinite of the Piemonte ophiolite nappe (NW Alps, Italy), is known for being very Fe-rich and Cr-free (Stella, 1921; Compagnoni *et al.*, 1979, 1981; Diella *et al.*, 1994; Rossetti *et al.*, 2009). This magnetite differs from apparently similar mineralizations of the adjacent Mt. Avic ultramafic massif (ore deposits of Lago Gelato, Ussel, and Valmeriana; *e.g.*, Stella, 1921; Rossetti *et al.*, 2009; Dal Piaz *et al.*, 2010) and other serpentinites of the Western Alps (*e.g.*, Lanzo Massif, Kaczmarek & Müntener, 2008 and references therein; Balangero, Rossetti & Zucchetti, 1988a and b), characterized by the

DOI: 10.1127/ejm/2014/0026-2410
0935-1221/14/0026-2410 $ 9.00

occurrence of magnetite with Cr-rich cores, suggesting growth after chromite contained within ultramafites (Diella *et al.*, 1994; Rossetti *et al.*, 2009; Della Giusta *et al.*, 2011) and/or relics of Cr-rich spinel. The recent mention of Cr-rich magnetite ($Cr_2O_3$ up to ~12 wt.%) found as micrometric idiomorphic crystals in serpentine in the Liconi mine, near Cogne (Martin *et al.*, 2009), has again raised the question of the possible metamorphic derivation of the Cogne magnetite from primary Cr-rich spinel as proposed by Diella *et al.* (1994).

The magnetite mineralization of Cogne is similar to those reported by Routhier (1963) in Corsica serpentinites and by Gahlan *et al.* (2006) in the hydrothermal deposit of Bou Azzer (Morocco). Enrichments in magnetite crystals are reported also in oceanic abyssal serpentinized peridotites (Alt & Shanks, 1998; Beard & Hopkinson, 2000; Bach *et al.*, 2006; Evans, 2011; Klein *et al.*, 2014). According to recent studies carried out in the Ocean Drilling Program (ODP) and the Deep Sea Drilling Project (DSDP), magnetite formation and peridotite serpentinization go hand-in-hand (*e.g.*, Mével, 2003; Bach *et al.*, 2006; Frost & Beard, 2007; Evans, 2011; Nadoll *et al.*, 2014). Other authors noticed a link between an exponential increase of magnetic susceptibility and the decrease in density of the abyssal peridotites undergoing hydration at mid-ocean ridges (Toft *et al.*, 1990; Dyment *et al.*, 1997; Klein *et al.*, 2014). Several studies were also focused on the hydrothermal fluids associated with serpentinization (*e.g.*, Charlou *et al.*, 1998; Beard & Hopkinson, 2000; Klein *et al.*, 2009; Jones *et al.*, 2010; Berndt *et al.*, 2014) and to metasomatic reactions (*e.g.*, Frost & Beard, 2007).

In this paper, we present new data on magnetite and associated minerals in the serpentinites of the Cogne mining area. As noted by Gahlan *et al.* (2006), very few analytical studies have been published on magnetite, in particular concerning detailed mineral- and crystal chemistry. Therefore, the first part of this paper deals with the characterization of the Cogne magnetite from the petrographic to the chemical and mineralogical point of view. In the second part, we report the investigation of microtextures and minerals associated with magnetite, *i.e.*, serpentine, garnet, pyroxene, chlorite and Fe-Ni sulphides. These data are of primary importance in order to envisage processes and environments of formation of this deposit, which are examined in the Discussion section. Abbreviations used for mineral names follow Whitney & Evans (2010).

## Geological outline and previous studies

The Cogne area has been the most famous iron mining district of the Alps since the 15th century (Jervis, 1873; Stella, 1921; Compagnoni *et al.*, 1979; Castello, 1981). It is located north of the Gran Paradiso massif (Fig. S1a and b freely available online as Supplementary Material linked to this article on the GSW website of the journal, http://eurjmin.geoscienceworld.org/). Magnetite was extracted from a mineralized lens associated with a serpentinite body 2.5 km long, embedded together with blueschist-facies calcschists and marbles of the Piemonte nappe (Aouilletta Unit, Dal Piaz *et al.*, 2010) along the southern Montzalet slope (Cogne Faisceau, Elter, 1971) (Fig. S1c), above the tectonic contact with the underlying Grivola-Urtier eclogitic unit (Dal Piaz *et al.*, 2010). Compagnoni *et al.* (1981) suggested that magnetite formation was related to the serpentinization of the mantle peridotite exhumed on the ocean floor of the Tethys, followed by Alpine metamorphism. The serpentinite extends from the Grauson valley (Larsinaz mine, altitude 1900 m) to the Grand'Eyvia valley where three main galleries (Costa del Pino, 2027 m a.s.l., Colonna, 2406 m a.s.l., and Liconi, 2520 m a.s.l.) were excavated across the serpentinite to attain the magnetite orebody. The exploitation of the Cogne orebody yielded around 15 million tons of magnetite (Bethaz, 1987), corresponding to 6 million tons of iron, between 1909 and 1979. Analyses by Stella (1921) on the ore mineral show Fe content ranging between 58 and 68 wt.% with an average content of 63 wt.%. Analyses by Compagnoni *et al.* (1979) on the coarse-grained magnetite, called ''cumulitic magnetite'' because of its resemblance to cumulitic chromite, show traces of Mg, Ca and Al, a low Ti content (140 ppm) and a very low Cr content (7 ppm), with more Co (570 ppm) and Zn (780 ppm). The very low amount of Cr is of particular interest because it differentiates the Cogne ore from other nearby magnetite mineralizations associated to serpentinites, *e.g.*, Plan des Tuves (Stella, 1921); Mt. Avic (Stella, 1921; Compagnoni *et al.*, 1979, 1981; Diella *et al.*, 1994; Rossetti *et al.*, 2009). According to Di Colbertaldo *et al.* (1967); Compagnoni *et al.* 1979, 1981) and Dal Piaz *et al.* (2010), the magnetite of the Cogne orebody is associated with low amounts of pyrite, chalcopyrite and pyrrhotite. Co-Ni sulphides and alloys have never been found in any of the previous studies, whereas they are common in the serpentinites of the Mt. Avic and in the Lanzo ultramafic massif (Rossetti & Zucchetti, 1988a and b; Zucchetti *et al.*, 1988; Diella *et al.*, 1994).

## Investigated samples and analytical methods

As described by previous authors (*e.g.*, Compagnoni *et al.*, 1979; Rossetti *et al.*, 2009), the Cogne ultramafic body is mostly composed of antigorite serpentinite variably enriched in magnetite passing, towards its margins, to Ca-rich rocks like garnet- and diopside-bearing serpentinite. Similar Ca-rich rocks, generally considered the product of intense metasomatism as a consequence of serpentinization of surrounding peridotite, are generally named rodingites (*e.g.*, Frost & Beard, 2007 and references therein); consequently, the term ''rodingitic serpentinite'' is adopted throughout this paper to describe serpentinites strongly enriched in diopside and garnet. A detailed description of the field relationships in the Cogne area is not within the scope of this paper. The study is instead focused on a few samples that, based on the petrographic study of a large number of samples from the entire Cogne area (*cf.* Martin

*et al.*, 2006), have been selected because they show peculiar features (*e.g.*, textural and/or mineralogical pre-metamorphic relics) or are representative of a rock- and/or mineralization-type. The studied rocks are (i) *serpentinite with pseudomorphic texture after oceanic peridotite* (sample CO15, hereafter named *pseudomorphic serpentinite*, Table 1; Fig. 1a); (ii) *rodingitic serpentinite* (sample CO14; Table 1; Fig. 1b); and (iii) *serpentinites rich in magnetite* (CO17, CO18, CO24, GP45) (Table 1; Fig. 1c and d). Rock samples were collected in the Costa del Pino, Colonna and Liconi mining areas (Fig. S1a). The selected samples were analysed using X-ray fluorescence (XRF), powder (XRPD) and single crystal X-ray diffraction, electron microprobe analysis and micro-Raman spectroscopy. Details of the analytical procedures and operating conditions are available as Supplementary Material.

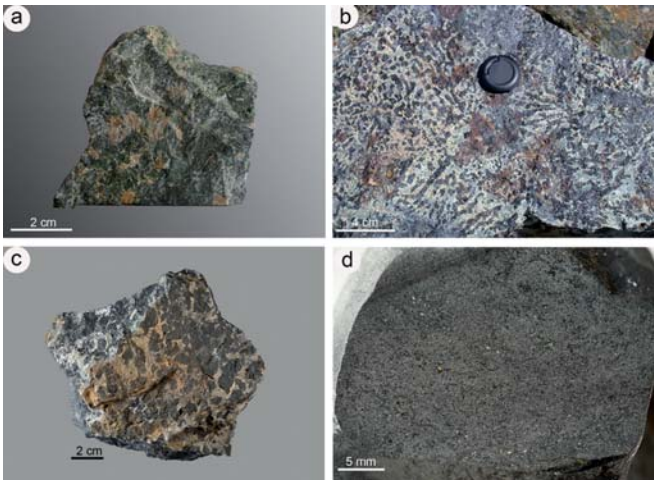


Fig. 1. Magnetite-bearing rocks. (a) Serpentinite with pseudomorphic texture after oceanic peridotite (CO15; Liconi gallery); (b) rodingitic serpentinite (CO14, from Liconi): cm-scaled aggregates of magnetite with radiating arrangement; (c) serpentinite with rounded black lenses of well crystallized magnetite (CO17, from Larsinaz); (d) serpentinite rich in mm-scaled magnetite (GP 45, from Grauson River). (online version in colour)

## Results

### Petrography of the magnetite-bearing rocks

A summary of the microtextures and mineral associations found in the investigated rocks is reported in Table 1. Below, we describe in detail the macro- and microscopic characters of the samples.

Pseudomorphic serpentinite CO15. The hand-specimen is a dark-green rock displaying mm-sized light brown rounded patches, crosscut by vein generations from mm- to sub mm- thickness (Fig. 1a). On the microscale, most of the rock is composed of serpentine (+ magnetite) with a relict mesh texture after olivine (Fig. 2a). The light brown

Table 1. Sample location, rock type, mineralogy, magnetite abundance, and general texture of the studied serpentinites.

| Sample | Mining site | Coordinates N | Coordinates E | Altitude | Serpentinite type | Mineralogy | Mag abundance | Main textural features |
|---|---|---|---|---|---|---|---|---|
| CO15 | Liconi | 45°36'45.2'' | 06°22'51.6'' | 2662 m | pseudomorphic | Srp + Mag (Cr-bearing) + Pn + Hzl ± Py ± Po | *ca.* 4 vol.% | Mesh-textured serpentinite with pseudomorphic texture after oceanic peridotite |
| CO14 | Liconi | 45°36'47.9'' | 07°23'46.6'' | 2484 m | rodingitic | Srp + Di + Adr + Chl + Mag (Cr-free) + Cal ± Ap | moderate | Fine-grained grano-lepidoblastic texture |
| CO17 | Larsinaz | 45°37'09.4'' | 07°22'38.7'' | 2300 m | magnetite-rich | Srp + Di + (OH)Adr + Mag (Cr-free) + Cal | high | Coarse-grained granoblastic Mag within intergranular Srp-Di-Adr-rich matrix |
| CO18 | Larsinaz | 45°37'08.3'' | 07°22'35.52'' | 1980 m | magnetite-rich | Srp + Di + Chl + Mag (Cr-free) ± Ap | high | Granoblastic Mag cemented by (and intergrown with) Srp-Di-Chl ± Ap |
| CO24 | Costa del Pino | 45°36'35.8'' | 07°22'40.6'' | 2010 m | magnetite-rich | Srp + Ol + Chl + Mag (Cr-free) + Brc ± Pn ± Hzl ± Po | high | Granoblastic Mag embedded in fine-grained Srp-Ol-Chl-Brc-rich matrix |
| GP45 | Grauson River | 45°37'7.98'' | 07°22'22.25'' | 1800 m | magnetite-rich | Srp + Mag (Cr-free) ± Brc | very high | Coarse-grained granoblastic Mag within intergranular Srp-Brc matrix |

Adr, andradite; Ap, apatite; Brc, brucite; Cal, calcite; Chl, chlorite; Di, diopside; Hzl, heazlewoodite; Mag, magnetite; Ol, olivine; Pn, pentlandite; Py, pyrite; Po, pyrrhotite; Srp, serpentine. Mineral abbreviations according to Whitney & Evans (2010).

patches correspond to bastitic pseudomorphs of serpentine and very fine-grained magnetite replacing primary mineral phases (probably orthopyroxene; Fig. 2b). Veins contain very fine-grained lizardite-rich matrix (no mesh texture) (see micro-Raman section) overgrown by idiomorphic, lamellar to prismatic, antigorite (Fig. 2c). Veins also contain bastitic intergrowth of mm- sized prismatic crystals completely replaced by orange to yellowish serpentine, mostly lizardite. The contact between the rock matrix and the veins is sharp. Locally, relics of dismembered matrix aggregates are found within the veins. Magnetite (*ca*. 4 vol.% of the rock) is heterogeneously distributed. Within the matrix, it occurs at the rims of olivine pseudomorphs as disseminations of irregularly shaped to rounded, 2–3 μm sized, grains (Fig. 2a). Where the pseudomorphic mesh texture is poorly preserved, magnetite is coarser grained (∼ 15–20 μm), subhedral and more abundant. Fine-grained magnetite disseminations also occur within bastitic pseudomorphs (Fig. 2b). Magnetite is instead a very minor phase within the veins (<<1 vol.%), where it occurs as scattered small grains (avg. 20 μm). Locally, larger grains occur (50–80 μm), often intergrown with euhedral antigorite (Figs. 2c and S2a). Sulphides (Figs. S2b and S2c, see composition in the mineral chemistry section), as rounded to irregularly shaped crystals, are heterogeneously distributed and <<1 vol.%. Their distribution in the matrix, though highly variable, broadly matches that of magnetite: where the pseudomorphic mesh texture is well preserved they are very fine-grained; they become more abundant and coarser-grained (∼ 30–100 μm) in portions where the mesh textures are poorly preserved. They are always intergrown with serpentine and magnetite. Sulphides are instead quite rare in the veins.

Rodingitic serpentinite CO14. The hand-specimen shows aggregates of magnetite with a radiating arrangement (Fig. 1b), embedded in a whitish matrix. The magnetite aggregates are mm-scaled and elongated, indicating an incipient foliation (Fig. 3a). Microscopically, magnetite appears recrystallized and contains inclusions of serpentine, calcite (Fig. 3b) and, occasionally, amoeboid inclusions of garnet. The light-coloured matrix is fine-grained and is composed of diopside, serpentine, calcite, garnet and chlorite. Diopside forms aggregates of mm-scaled idiomorphic crystals (Fig. 3b) enclosing prismatic serpentine, garnet and trails of fluid inclusions. Serpentine is present in elongated crystals, commonly prismatic if enclosed in pyroxene, or nearly lamellar if enclosed in garnet and magnetite. Garnet in the matrix is found in polygonal aggregates including serpentine. Interstices in garnet aggregates are commonly filled by magnetite. Chlorite is a minor phase; when present in idiomorphic crystals (∼1 mm), it shows bending and undulatory extinction. Among accessory minerals, apatite occurs within the serpentine–-garnet matrix. Mineral quantities in this rock were determined by X-ray powder diffraction: diopside 55 wt.%, calcite 15 wt.%, magnetite 15 wt.%, andradite 8 wt.% and antigorite 7 wt.%.

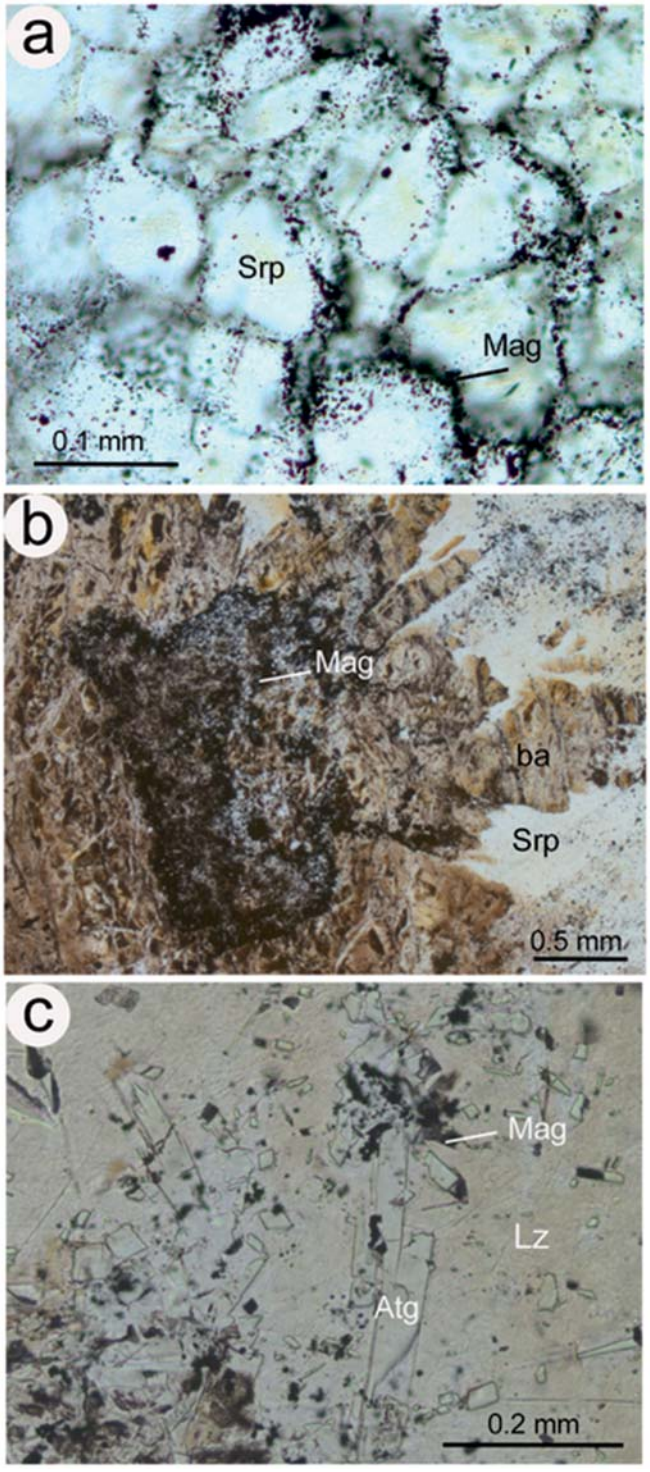


Fig. 2. Photomicrographs of pseudomorphic serpentinite (CO15). (a) Serpentinite, relict mesh texture: olivine is completely replaced by serpentine and very fine-grained magnetite disseminations occur at mesh rims. (b) Serpentinite, detailed view of a bastitic intergrowth (ba) replacing primary silicates (probably orthopyroxene); such intergrowth contains a concentration of very fine-grained magnetite, in part chromiferous (grains D1-D5 in Table 3). (c) Vein, very fine-grained lizardite matrix overgrown by prismatic antigorite; scattered magnetite also occurs. (online version in colour)

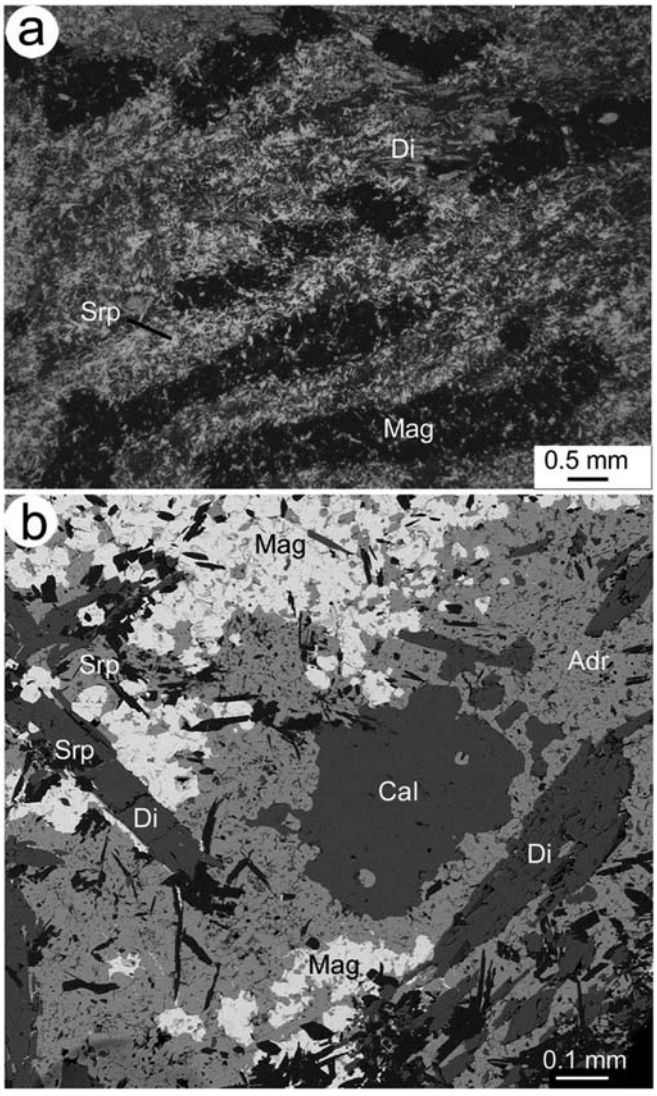


Fig. 3. Petrographic features in rodingitic serpentinite CO14. (a) Elongated magnetite aggregates in matrix composed of diopside, garnet and serpentine (transmitted light); (b) back-scattered electron image of magnetite aggregates in matrix composed of andradite, idiomorphic crystals of diopside and elongated, prismatic to lamellar, serpentine. Calcite is present in poikilitic crystals included in andradite.

Serpentinites rich in magnetite. Hand-specimen CO17 shows subhedral mm-sized magnetite in a whitish matrix (Fig. 1c). Microscopically, magnetite cores contain prismatic inclusions of serpentine, tiny serpentine fibres (Fig. S3a) and negative crystals. Subhedral diopside contains small inclusions of calcite, magnetite, serpentine, and garnet. Garnet commonly seals fractures within the magnetite crystals and is associated with calcite and minor serpentine. Additionally, it may occur intergrown with diopside and serpentine within magnetite crystals (Fig. S3b) or may be present as skeletal relics within diopside in contact with magnetite. Sample CO18 is characterized by sub-mm sized aggregates of magnetite crystals embedded in a coarse-grained matrix of serpentine, minor diopside, chlorite and apatite. Typical associations are serpentine + chlorite and chlorite + diopside. Serpentine is always euhedral and prismatic when associated with chlorite. Diopside appears subhedral to anhedral. Chlorite is present in large (up to 1 mm) fan-shaped crystals. In sample CO24, recrystallized magnetite occurs in the form of rounded aggregates of small crystals (up to a few mm in size) embedded in a brownish matrix composed of serpentine, chlorite, olivine and brucite (see micro-Raman section). Olivine occurs as small rounded μm-scaled grains dispersed in the serpentine matrix. Brucite and chlorite are also included as euhedral crystals in large magnetite crystals. Brucite can in turn include serpentine. Sulphides are present in very low amount, apart from very fine-grained pyrrhotite and pentlandite (± heazlewoodite) inclusions in magnetite. Sample GP45 was collected from the Grauson River near Gimillian (Fig. S1a). The rock is composed of mm-scaled magnetite in very high amounts in a serpentine and brucite matrix (Fig. 1d).

## Composition of the magnetite-bearing rocks

Whole-rock X-ray fluorescence analyses of the selected samples are reported in Table 2. Serpentinites show a large variation in $Fe_2O_3$ contents, from 6.75 wt.% $Fe_2O_3$ in pseudomorphic serpentinite CO15 to 79.1 wt.% $Fe_2O_3$ in magnetite-rich serpentinite CO18, reflecting the relative abundance of magnetite (Table 1). Therefore, the higher the $Fe_2O_3$ the lower the $SiO_2$ content (38.2 wt.% in sample CO15, and 9.69 wt.% in sample CO18) and the MgO content as well (38.5 wt.% in CO15, and 8.30 wt.% in CO18). In sample CO15, the loss-on-ignition value is high (13.7 wt.%), revealing the high amount of serpentine and the high degree of hydration of the rock. Rodingitic serpentinite CO14 shows a high Ca content (12.7 wt.% CaO), reflecting the abundance of diopside, andradite and calcite. All of the analysed rocks have very low $TiO_2$ content ($\leq$0.04 wt.%). Concerning minor and trace elements, Cr, Ni, S and Pb are relevant in pseudomorphic serpentinite CO15 (2389, 2387, 718, and 262 ppm, respectively); S and Ni are clearly a proxy for the occurrence of Fe-Ni sulphides, whereas Cr is related to the occurrence of Cr-rich magnetite (see below). The high contents of Co in magnetite-rich serpentinites CO24 and CO18, 358 and 333 ppm, respectively, confirm the abundance of magnetite in these samples.

## Mineral chemistry of magnetite

In rodingitic serpentinite and serpentinites rich in magnetite, magnetite compositions are characteristically Cr-free, homogeneous and very similar to those already known for the Cogne ore mineral (Stella, 1921; Compagnoni *et al.*, 1979; Diella *et al.*, 1994; Rossetti *et al.*, 2009). Average compositions are listed in Table 3. Iron is the only trivalent ion present in the ideal quantity (2.000 atoms per formula unit (apfu)). The only appreciable substitutions are those of the divalent iron $Fe^{2+}$ by Mg (minimum $\sim$ 0.02 apfu in

Table 2. Whole-rock analyses of pseudomorphic serpentinite (CO15), rodingitic serpentinite (CO14) and serpentinites rich in magnetite (CO18, CO24).

| wt.% | CO15 | CO14 | CO18 | CO24 |
|---|---|---|---|---|
| $SiO_2$ | 38.22 | 35.24 | 9.69 | 15.11 |
| $TiO_2$ | 0.02 | 0.02 | 0.02 | 0.04 |
| $Al_2O_3$ | 0.97 | 0.45 | 0.38 | 0.30 |
| $Fe_2O_3$ | 6.75 | 27.36 | 79.08 | 54.72 |
| MnO | 0.12 | 0.20 | 0.34 | 0.46 |
| MgO | 38.49 | 19.10 | 8.30 | 21.28 |
| CaO | 0.07 | 12.67 | 1.75 | 0.10 |
| $Na_2O$ | 0.03 | 0.01 | 0.01 | 0.01 |
| $K_2O$ | 0.01 | 0.01 | 0.01 | 0.01 |
| $P_2O_5$ | 0.01 | 0.01 | 0.01 | 0.03 |
| L.O.I. | 13.65 | 4.95 | 0.04 | 7.56 |
| Total | 98.33 | 100.00 | 99.62 | 99.61 |
| ppm | | | | |
| S | 718 | 50 | 117 | 212 |
| Sc | 22 | <5 | <5 | 9 |
| V | 34 | 10 | 25 | 19 |
| Cr | 2389 | 9 | 8 | 26 |
| Co | 125 | 120 | 333 | 358 |
| Ni | 2387 | 106 | 85 | 29 |
| Cu | 9 | 26 | 81 | 23 |
| Zn | 54 | 61 | 95 | 121 |
| Ga | <5 | <5 | 7 | <5 |
| Rb | 5 | 6 | 9 | 8 |
| Sr | 3 | 10 | 4 | 6 |
| Y | 5 | <3 | <3 | <3 |
| Zr | 9 | 10 | 35 | 16 |
| Nb | 3 | <3 | <3 | <3 |
| Ba | <10 | <10 | <10 | <10 |
| La | <10 | <10 | 12 | 26 |
| Ce | <10 | 13 | 21 | <10 |
| Nd | 21 | 29 | 37 | 31 |
| Pb | 262 | <5 | <5 | <5 |
| Th | <3 | 10 | 10 | 11 |
| U | <3 | <3 | <3 | 4 |

CO14 B, maximum ~ 0.15 apfu in GP45) and by minor amounts of Mn (up to ~0.02 apfu). Ti content is quite low (≤0.001 apfu). The Mg content determined is in agreement with that already reported for Cogne magnetite (0.3–8.0 wt.% MgO) (*e.g.*, Stella, 1921; Compagnoni *et al.*, 1979; Rossetti *et al.*, 2009; Della Giusta *et al.*, 2011).

In contrast with Cr-free magnetite, presumed to be distinctive of Cogne in earlier studies, we will show that magnetite can contain high amounts of Cr. In pseudomorphic serpentinite, magnetite was analysed in different microtextural sites corresponding both to mesh textures after olivine (B, C, E, Table 3; Fig. 2a) and to bastites after orthopyroxene (A, D, Table 3; Fig. 2b). Magnetite compositions are highly variable (Table 3). In particular, X-ray maps show that crystals are highly zoned in Cr (Fig. 4). Magnetite cores are almost Cr free, surrounded by Cr rich euhedral rims (up to 17.0 wt.% $Cr_2O_3$), mantled in turn by partially resorbed magnetite characterized by ~2.0 wt.% $Cr_2O_3$ (Table S1). In all analyses, Cr is positively correlated with Mn and negatively correlated with Fe. Additionally, Ni and Mn contents are on average 0.007 apfu and ~0.020 apfu, respectively, both higher than in Cr-free magnetite. Zn content is quite variable. Chromium is clearly negatively correlated with $Fe^{3+}$ (Fig. 5a) and $Fe^{2+}$ (Fig. 5b) and positively correlated with Mn (Fig. 5c) and Zn (Fig. 5e). From Cr-bearing magnetite in pseudomorphic serpentinite to Cr-free magnetite in rodingitic serpentinite, we can follow, with decreasing Cr (or increasing $Fe^{3+}$), the compositional changes occurring in the Cogne magnetite: $Fe^{3+}$ substitutes Cr, and $Fe^{2+}$ substitutes the divalent ions Mn, Zn and Ni. These substitutions can be described by the exchange vectors $Fe^{3+}$ $Fe^{2+}$ $Cr^{3+}_{-1}$ (Mn, Zn, Ni) $^{2+}_{-1}$. Conversely, Mg substituting $Fe^{2+}$ is always appreciable and independent of Cr content (Fig. 5f). The Cogne Cr-free magnetites can thus be defined as members of the magnetite–magnesioferrite series with compositions close to pure magnetite (2–15 mol.% $MgFe_2O_4$). Magnesium in magnetite also influences the cation distribution, as shown below.

## Crystal chemistry of magnetite

The first crystal-structure refinements of pure (Cr-free) magnetite from Cogne were performed by Rossetti *et al.* (2009) together with Cr-spinels from Mt. Avic.

For our study, structural investigations were undertaken by means of single-crystal X-ray diffraction to determine the two independent geometric variables: the cell parameter (*a*) and the oxygen position parameter (*u*) (Table S4). The two single crystals studied here are derived from Cr-free magnetite aggregates and mm-scaled blasts in serpentinites rich in magnetite, CO24 and GP45. In the magnetite crystal structure, the tetrahedral site is predominantly occupied by $Fe^{3+}$ (inverse structure), and the octahedral sites are occupied by both $Fe^{2+}$ and $Fe^{3+}$. Conversely, in chromite, for example, the tetrahedral site is predominantly occupied by $Fe^{2+}$ (normal structure). The spinel structures are generally largely inverse or largely normal rather than completely of one type or the other, the dominant ion in a given site being present at a maximum of ~95 %.

The spinel cell parameter (*a*) is quite sensitive to chemical composition (Hill *et al.*, 1979) and is an increasing function of both tetrahedral and octahedral bond distances (Hafner, 1960). The cell parameter values (*a*) are: $a = 8.398(4)$ Å for magnetite crystal from sample CO24, and $a = 8.401(3)$ Å for magnetite crystal from sample GP45 (Table S4), both of them just slightly higher than in pure magnetite ($a$ = 8.3949 Å, Nakagiri *et al.*, 1986) (see Supplementary Material for details of cell parameter measurements). After the X-ray data collection, the two magnetite crystals from samples CO24 and GP45 were analysed with the electron microprobe (Table 3).

Besides the cell parameter, the structural investigations allowed the determination of (i) the tetrahedral and octahedral bond distances (and thus, inverse or normal structure) by means of the oxygen position parameter *u* (Table S4) and (ii) the possible presence of atomic species replacing Fe, by means of the refined tetrahedral- and octahedral-site occupancies. In the single crystals studied here, the tetrahedral site is fully occupied by Fe atoms (site

Table 3. Representative microprobe analyses of magnetite in pseudomorphic serpentinite CO15, and average compositions of magnetite in rodingitic serpentinite CO14 and in serpentinites rich in magnetite (CO17, CO18, CO24, GP45). Number in parentheses refers to standard deviation.

| | CO15 | | | | | | | | | | CO14 | CO14 | | | | CO24 | GP45 |
|---|---|---|---|---|---|---|---|---|---|---|---|---|---|---|---|---|---|
| | B | C-1 | C-2 | C-3 | E | A | D-1 | D-3 | D-4 | D-5 | A | B | CO17 | CO18 | CO24 | single cryst. | single cryst. |
| wt.% | in mesh-texture | | | | | in bastite | | | | | av. (21) | av. (3) | av. (20) | av. (9) | av. (54) | av. (38) | av. (4) |
| MgO | 1.66 | 2.01 | 1.68 | 1.71 | 3.44 | 2.09 | 1.60 | 2.78 | 1.96 | 2.18 | 2.07 (24) | 0.37 (1) | 0.85 (18) | 1.13 (10) | 2.12 (12) | 1.69 (10) | 2.74 (11) |
| $Al_2O_3$ | 0.02 | 0.02 | 0.01 | 0.03 | 0.03 | 0.02 | 0.01 | 0.08 | 0.06 | 0.03 | 0.04 (5) | 0.03 (4) | 0.01 (2) | 0.04 (4) | 0.08 (5) | 0.10 (4) | 0.02 (2) |
| $SiO_2$ | 0.40 | 0.55 | 0.30 | 0.34 | 0.16 | 0.39 | 0.24 | 0.48 | 0.34 | 0.25 | 0.08 (8) | 0.08 (1) | 0.07 (9) | 0.06 (6) | 0.04 (4) | 0.05 (7) | 0.07 (1) |
| CaO | n.d. | n.d. | n.d. | n.d. | 0.01 | n.d. | n.d. | n.d. | n.d. | n.d. | n.d. | 0.21 (5) | 0.03 (5) | 0.02 (4) | n.d. | n.d. | n.d. |
| $TiO_2$ | 0.00 | 0.03 | 0.01 | 0.00 | 0.12 | 0.02 | 0.01 | 0.02 | 0.02 | 0.03 | 0.01 (1) | b.d.l. | 0.02 (1) | 0.03 (2) | 0.05 (2) | 0.04 (2) | 0.01 (2) |
| $Cr_2O_3$ | 1.09 | 2.45 | 1.57 | 2.03 | 17.01 | 0.35 | 0.02 | 9.99 | 3.32 | 7.37 | 0.01 (1) | b.d.l. | 0.01 (1) | 0.01 (1) | 0.01 (1) | 0.01 (2) | 0.01 (2) |
| MnO | 0.30 | 0.52 | 0.35 | 0.41 | 3.09 | 0.27 | 0.25 | 2.13 | 0.69 | 1.62 | 0.55 (5) | 0.37 (33) | 0.41 (4) | 0.39 (4) | 0.58 (8) | 0.69 (3) | 0.31 (6) |
| FeO | 27.98 | 27.27 | 27.90 | 27.92 | 22.68 | 27.64 | 28.07 | 23.66 | 26.82 | 25.23 | 27.22 (49) | 30.02 (11) | 29.68 (24) | 29.08 (19) | 27.16 (19) | 27.70 (16) | 26.81 (18) |
| NiO | 0.23 | 0.25 | 0.24 | 0.27 | n.d. | 0.16 | 0.12 | 0.26 | 0.24 | 0.24 | 0.05 (3) | 0.06 (4) | 0.02 (2) | 0.03 (3) | 0.02 (2) | 0.02 (3) | 0.04 (4) |
| ZnO | 0.01 | 0.04 | 0.01 | 0.04 | n.d. | 0.01 | 0.22 | 0.35 | 0.09 | 0.29 | 0.03 (3) | 0.01 (1) | 0.02 (3) | 0.02 (2) | 0.03 (3) | 0.03 (4) | 0.06 (8) |
| $Fe_2O_3$ | 66.61 | 64.68 | 66.69 | 66.45 | 51.75 | 68.14 | 68.64 | 56.37 | 64.16 | 60.17 | 69.58 (35) | 69.34 (39) | 70.01 (35) | 69.62 (43) | 69.62 (30) | 69.35 (34) | 70.87 (23) |
| Total | 98.31 | 97.81 | 98.76 | 99.21 | 98.29 | 99.09 | 99.18 | 96.10 | 97.70 | 97.40 | 99.63 | 100.50 | 101.13 | 100.42 | 99.70 | 99.67 | 100.93 |
| for 4 oxygens: | | | | | | | | | | | | | | | | | |
| Mg | 0.095 | 0.116 | 0.096 | 0.098 | 0.194 | 0.119 | 0.091 | 0.161 | 0.113 | 0.126 | 0.117 (14) | 0.021 (1) | 0.048 (10) | 0.064 (5) | 0.120 (7) | 0.096 (6) | 0.153 (6) |
| Al | 0.001 | 0.001 | 0.000 | 0.001 | 0.001 | 0.001 | 0.001 | 0.003 | 0.003 | 0.001 | 0.002 (2) | 0.002 (2) | 0.001 (1) | 0.002 (2) | 0.004 (2) | 0.004 (2) | 0.001 (1) |
| Si | 0.016 | 0.021 | 0.012 | 0.013 | 0.006 | 0.015 | 0.009 | 0.019 | 0.013 | 0.010 | 0.003 (3) | 0.003 (0) | 0.003 (3) | 0.002 (2) | 0.002 (1) | 0.002 (3) | 0.003 (1) |
| Ca | | | | | 0.000 | | | | | | | 0.009 (2) | 0.001 (2) | 0.001 (2) | | | |
| Ti | 0.000 | 0.001 | 0.000 | 0.000 | 0.003 | 0.001 | 0.000 | 0.001 | 0.001 | 0.001 | 0.000 (0) | | 0.001 (0) | 0.001 (1) | 0.001 (1) | 0.001 (0) | 0.000 (0) |
| Cr | 0.033 | 0.076 | 0.048 | 0.062 | 0.508 | 0.010 | 0.000 | 0.308 | 0.102 | 0.226 | 0.000 (0) | | 0.000 (0) | 0.000 (0) | 0.000 (0) | 0.000 (0) | 0.000 (1) |
| Mn | 0.010 | 0.017 | 0.012 | 0.013 | 0.099 | 0.009 | 0.008 | 0.070 | 0.023 | 0.053 | 0.018 (2) | 0.012 (10) | 0.013 (1) | 0.012 (1) | 0.019 (3) | 0.022 (1) | 0.010 (2) |
| $Fe^{2+}$ | 0.903 | 0.880 | 0.897 | 0.893 | 0.717 | 0.883 | 0.900 | 0.770 | 0.868 | 0.816 | 0.866 (15) | 0.959 (10) | 0.939 (8) | 0.924 (3) | 0.863 (6) | 0.883 (5) | 0.838 (4) |
| Ni | 0.007 | 0.008 | 0.008 | 0.008 | | 0.005 | 0.004 | 0.008 | 0.008 | 0.007 | 0.001 (1) | 0.002 (1) | 0.000 (0) | 0.001 (1) | 0.000 (1) | 0.001 (1) | 0.001 (1) |
| Zn | 0.000 | 0.001 | 0.000 | 0.001 | | 0.000 | 0.006 | 0.010 | 0.003 | 0.008 | 0.001 (1) | 0.000 (0) | 0.001 (1) | 0.000 (1) | 0.001 (1) | 0.001 (1) | 0.002 (2) |
| $Fe^{3+}$ | 1.935 | 1.879 | 1.928 | 1.911 | 1.471 | 1.958 | 1.980 | 1.650 | 1.868 | 1.752 | 1.992 (8) | 1.993 (2) | 1.993 (7) | 1.991 (6) | 1.990 (5) | 1.989 (6) | 1.993 (2) |
| Sum | 3.000 | 3.000 | 3.000 | 3.000 | 3.000 | 3.000 | 3.000 | 3.000 | 3.000 | 3.000 | 3.000 | 3.000 | 3.000 | 3.000 | 3.000 | 3.000 | 3.000 |

In labels of sample CO15, letter (A-E) refers to micro-site, last digit refers to grain; n.d.: not determined; b.d.l.: below detection limit.

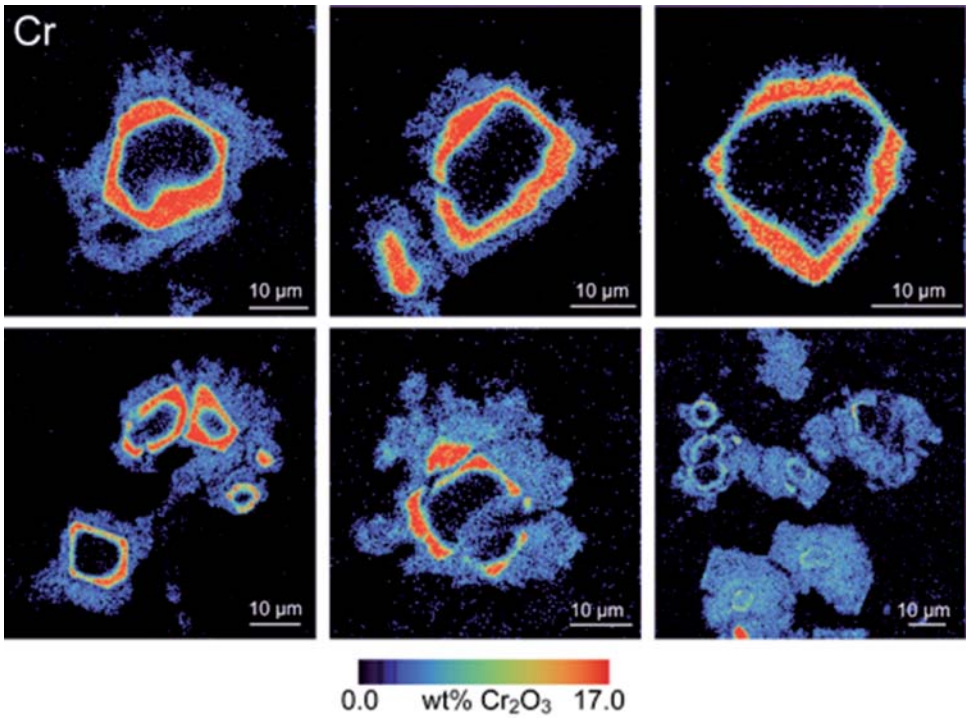


Fig. 4. Colorized X-ray maps of Cr in magnetite (pseudomorphic serpentinite CO15). Crystals display oscillatory zoning, with Cr poor cores (*ca*. 0.3-0.4 wt.% $Cr_2O_3$) mantled by Cr rich euhedral rims (*ca*. 17.0 wt.% $Cr_2O_3$), in turn surrounded by subhedral magnetite characterized by *ca*. 2.0 wt.% $Cr_2O_3$. (online version in colour)

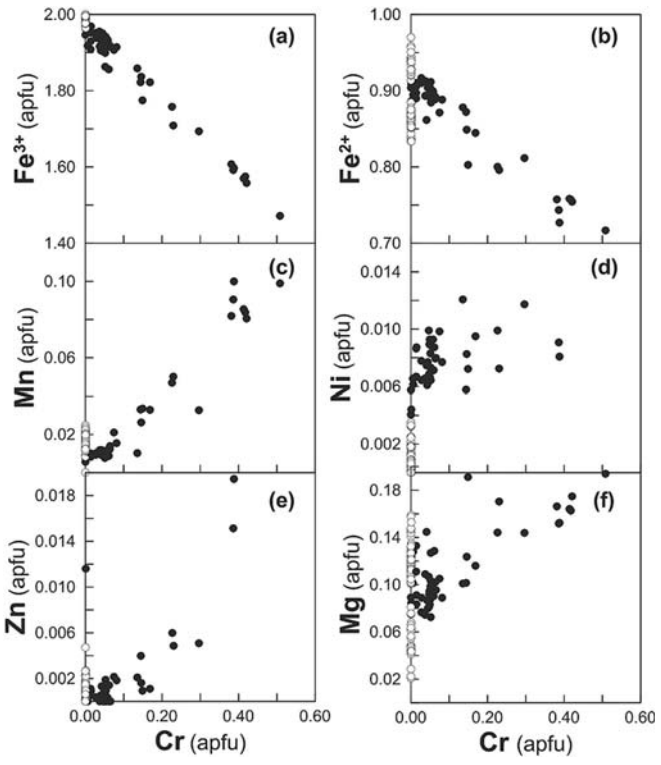


Fig. 5. Diagrams Cr *vs.* $Fe^{3+}$ (a), *vs.* $Fe^{2+}$ (b), *vs.* Mn (c), *vs.* Ni (d), *vs.* Zn (e), *vs.* Mg (f) (apfu: atoms per formula unit) showing the Cogne magnetites characteristics (all point analyses: Tables S1, S2, and S3). Filled circles: Cr-bearing magnetites (CO15). Open circles: Cr-free magnetites (CO14, CO17, CO18, CO24, GP45).

occupancy $\sim$ 1.00, Table S4), whereas Fe occupancy in the octahedral site is $<$ 1.00, indicating that the Mg atoms present in the Cogne magnetite (Mg $\sim$ 0.10 apfu in CO24; $\sim$ 0.15 apfu in GP45; Table 3) are mainly situated here. According to the procedure described in Della Giusta *et al.* (2011), the crystal-chemical formulae of the two investigated crystals are calculated as:

$$^{IV}\left(Fe^{3+}_{0.91}Fe^{2+}_{0.09}\right)^{VI}\left(Fe^{3+}_{1.08}Fe^{2+}_{0.76}Mg_{0.15}Mn_{0.01}\right)O_4$$

for single crystal GP45, and

$$^{IV}\left(Fe^{3+}_{0.91}Fe^{2+}_{0.07}Mg_{0.02}\right)^{VI}\left(Fe^{3+}_{1.08}Fe^{2+}_{0.82}Mg_{0.08}Mn_{0.02}\right)O_4$$

for single crystal CO24.

Also in these two magnetites, the occupancy of the dominant tetrahedral $Fe^{3+}$ is $\sim$ 90 % (largely, but not completely, inverse structure); small quantities of the divalent iron also remain in this site. These data compare well with those already reported for the Cogne magnetite by Rossetti *et al.* (2009) and by Della Giusta *et al.* (2011). Both $Fe^{2+}$ in magnetite and Mg in magnesioferrite have a strong preference for the octahedral site.

Cogne magnetites were compared with the spinels from Mt. Avic serpentinite massif. The affinity in composition between them is shown in the Cr *vs.* $Fe^{3+}$ trend (Fig. 6a). However, there are some appreciable and intriguing differences:

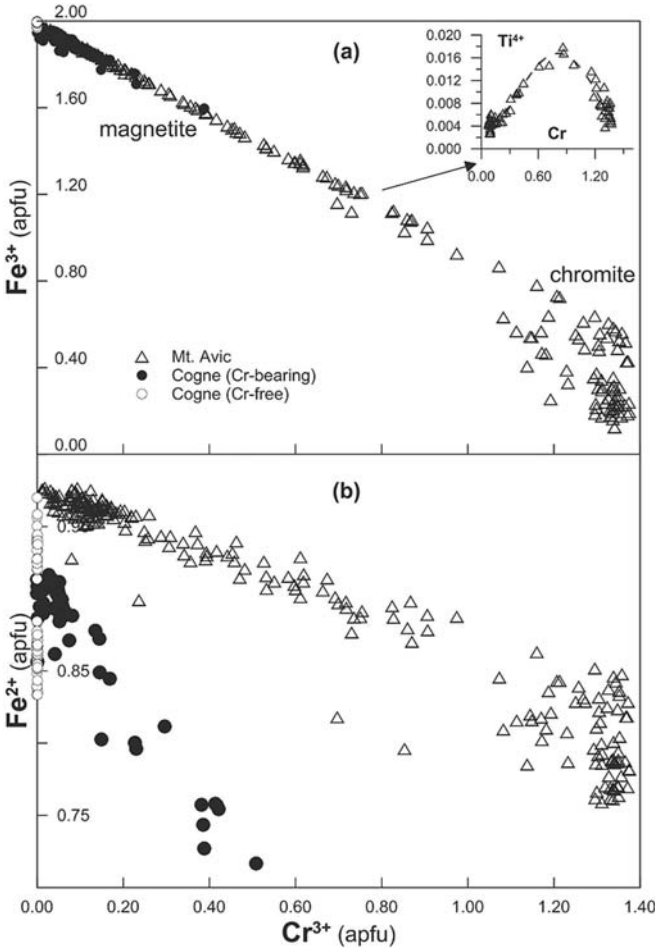


Fig. 6. Diagram showing Cr *vs.* $Fe^{3+}$ (a), and Cr *vs.* $Fe^{2+}$ (b) (apfu: atoms per formula unit) in spinels from Cogne, this study (filled circles, Cr-bearing magnetites; open circles, Cr-free magnetites), and from Mt. Avic serpentinites (triangles) (Rossetti *et al.*, 2009; Della Giusta *et al.*, 2011).

(1) Chromite relics are abundant in the spinel grains from the Mt. Avic (Diella *et al.*, 1994; Fontana *et al.*, 2008; Rossetti *et al.*, 2009; Della Giusta *et al.*, 2011); thus, the chromite to magnetite transformation can be followed starting from the most Cr-rich (*i.e.*, Cr $\sim$ 1.4 apfu; normal structure) to the almost Cr-free compositions (inverse structure) (Fig. 6a). The transition from chromite, *e.g.*:

$$^{IV}\left(Fe^{2+}_{0.9}\,Fe^{3+}_{0.1}\right)^{VI}\left(Cr^{3+}_{1.3}Fe^{3+}_{0.6}Fe^{2+}_{0.1}\right)O_4,$$

to chromian magnetite, *e.g.*:

$$^{IV}\left(Fe^{2+}_{0.1}Fe^{3+}_{0.9}\right)^{VI}\left(Cr^{3+}_{0.3}Fe^{3+}_{0.8}Fe^{2+}_{0.9}\right)O_4,$$

implies a complete redistribution of the cations between the tetrahedral and octahedral sites. Moreover, in the Mt. Avic spinels, this transformation is also accompanied by a symmetric change in Ti content, yielding a bell-shaped trend (Fig. 6a, inset). As described by Della Giusta *et al.* (2011), the $R^{2+}{}_2TiO_4$ component increases, going from chromite to magnetite, favouring the transition from normal to inverse structure.

(2) In the Cogne mineralization, chromite relics have never been found; our data show that the Cr *vs.* $Fe^{3+}$ trend starts at chromian magnetite (*i.e.*, Cr $\sim$ 0.5 apfu) rather than at chromite, and ends up at pure magnetite. Moreover, Fig. S4a shows the quite low content of Ti in all of the Cogne magnetite compositions.

(3) Cogne magnetite compositions are poorer in $Fe^{2+}$ (Table 3; Fig. 6b) and richer in Mn and Mg (Fig. S4b,c) than the Cr-bearing magnetite from Mt. Avic. This characteristic also constrains the intracrystalline cation distribution: less $Fe^{2+}$ in the M site means less $Fe^{3+}$ necessary for $Fe^{2+}$-$Fe^{3+}$ electron hopping (Verwey & de Boer, 1936). Consequently, $Fe^{3+}$ in excess of that necessary for electron hopping gives higher values to iron formal valence with respect to Cr-magnetites from Mt. Avic. This appears to be the main characteristic of all of the refined magnetite structures from Cogne.

## Chemistry of other minerals

*Serpentine.* In pseudomorphic serpentinite CO15 the micro-Raman and mineral-chemistry data clearly reveal the occurrence of serpentines with different structures and composition (Fig. 7, Table 4). Within the mesh-textures, the serpentine replacing olivine is mainly lizardite, as shown by Raman peaks at 690 $\pm$ 2 $cm^{-1}$ and at around 385 $cm^{-1}$ (Fig. 7a). The position of the latter peak (which is at 388 $cm^{-1}$ in Al-free lizardite) suggests the occurrence of some Al substitution, in agreement with the mineral-chemistry data. Lizardite found in the mesh-textures (Table 4, column 1) is characterized by Si lower than 2 apfu and Al $\geq$ 0.1 apfu, so part of the Al is used to fill the tetrahedral sites (*e.g.*, Mellini & Viti, 1994; Viti & Mellini, 1998; Mével, 2003; Rinaudo *et al.*, 2003). It is the most Al- and $Fe^{2+}$-rich among the CO15 serpentines. Additionally, it contains small amounts of Cr, but lacks Ni, Ti, and Ca. The mesh-like lizardite is overgrown and commonly rimmed by antigorite (diagnostic Raman peaks at 684–685 and 1045 $cm^{-1}$, Fig. 7b). Antigorite (column 2 in Table 4) is characterized by Si higher than 2 apfu and by a sum of octahedral cations significantly lower than 3 apfu, with a Mg/Si ratio lower than lizardite (Fig. S5). The bastitic intergrowths replacing orthopyroxene are also composed of very fine-grained lizardite, brownish to white in colour; it shows Si lower than 2 apfu, and extremely low Al present (Table 4, column 3), indicating that $Fe^{3+}$ could substitute Si in the tetrahedral sites (see also Rozenson *et al.*, 1979; Wicks & O'Hanley, 1988; Klein *et al.*, 2009); the presence of $Fe^{3+}$ is also suggested by the sum of cations exceeding 5 per 7 oxygens when assuming all iron as $Fe^{2+}$(Table 4). It contains small amounts of Ni but lacks Cr. The intergrowths are crosscut by very thin (up

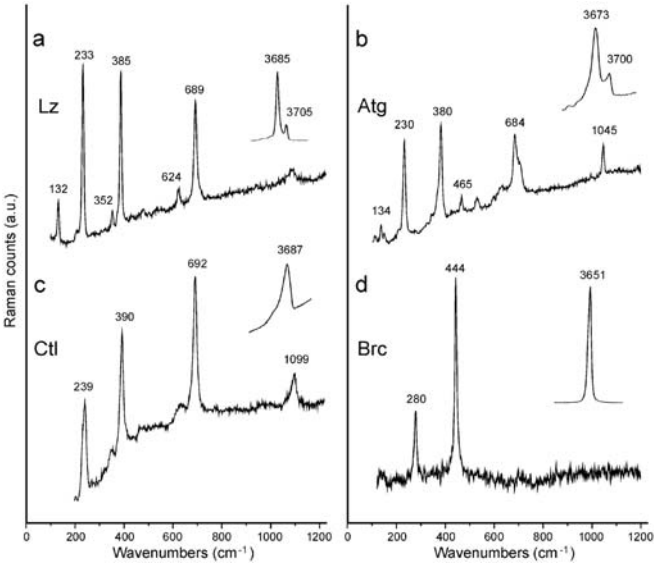


Fig. 7. Selected micro-Raman spectra from the Cogne serpentinite. For all spectra, the relevant peaks in the high-wavenumber region are also shown. (a) mesh-textured lizardite; (b) neoblastic antigorite overgrowing lizardite; (c) chrysotile veinlet within a bastitic intergrowth after orthopyroxene; (d) coarse-grained brucite. a–c, sample CO15, d, sample CO24.

to ~ 3 μm thick) veinlets composed alternatively of lizardite (generally Al-poor) or chrysotile (Fig. 7c). When cross-cutting relationships are observed, chrysotile postdates lizardite. Within the larger veins, the very fine-grained serpentine groundmass is mainly composed of lizardite. The position of the $SiO_4$ tetrahedra bending modes (387–388 $cm^{-1}$) suggests a low Al content. Locally, the shift of the peak up to 390 $cm^{-1}$ suggests the occurrence of very fine-grained chrysotile intergrown with lizardite. The groundmass is overgrown by prismatic antigorite, showing the same chemical composition as antigorite in the host serpentinite. The orange to yellowish serpentine overgrowing the prismatic crystals in the veins is composed of lizardite, whose composition matches that of lizardite from the bastitic intergrowths replacing orthopyroxene described above. It is crosscut by different generations of micrometre-thick veinlets of lizardite and locally, chrysotile.

The presence of both antigorite and chrysotile in the Cogne mineralized rocks was already reported by Compagnoni *et al.* (1979); Diella *et al.* (1994), and Rossetti *et al.* (2009), and that of antigorite by Di Colbertaldo *et al.* (1967). Conversely, the occurrence of lizardite has never been reported previously.

In rodingitic serpentinite CO14, X-ray powder diffraction and micro-Raman analyses confirm that serpentine is mainly antigorite. Two distinctive compositions are reported in Table 4. One, relative to serpentine associated to diopside, is characterized by Si in excess of 2 apfu and with an octahedral sum significantly lower than 3 apfu (column 5). Additionally, small amounts of Ca are detected (0.013 apfu), but the large standard deviation may indicate a mixed analysis with Ca-rich minerals (*e.g.*, calcite, diopside). The other (column 4), relative to μm-scaled euhedral lamellar serpentine enclosed in garnet and magnetite, is characterized by higher Al and Fe, and lower Si contents than the first one. However, the presence of a small peak at 382–383 $cm^{-1}$ in some antigorite spectra suggests the occurrence of antigorite + lizardite intergrowths, at least locally.

In serpentinite rich in magnetite CO17, micro-Raman analyses on serpentine show spectra typical of antigorite, commonly intergrown with chlorite and, locally, diopside. As in sample CO14, antigorite is present with two compositions, distinctive for Si and Al. The one generally associated with magnetite and garnet has the highest $Fe^{2+}$ content (0.130 apfu; Table 4, column 6) among the studied serpentines. Serpentine enclosed in diopside shows relevant $Fe^{2+}$ as well (0.091 apfu; column 7) but lower Al and higher Si contents than the first one. In sample CO18, serpentine (antigorite, column 8) is quite similar to one of the antigorites in sample CO17 (*i.e.*, column 7). In sample CO24, two types of serpentine are recognizable, both well crystallized in the matrix. Rather low Al and Fe contents (Table 4, column 9) correspond to antigorite, while lizardite (column 10) is quite similar to that of column 3 in sample CO15 (*i.e.*, very low Al content and probably tetrahedral $Fe^{3+}$). The microstructural observations clearly show that antigorite overgrows lizardite.

To summarize the analysis of the serpentines, the most Fe-rich serpentine ($Fe^{2+} = 0.130$ apfu) is found in sample CO17, namely the serpentine generally associated with magnetite and garnet. Ni is detected in trace amounts (0.003 apfu) only in lizardite of the pseudomorphic serpentinite CO15, characterized by a very low Al content (0.005 apfu) and probably by tetrahedral $Fe^{3+}$. Additionally, only in sample CO15, Cr is detected (~ 0.01 apfu), both in the mesh-like lizardite and in the antigorite neoblasts.

*Garnet*. In rodingitic serpentinite CO14 and in serpentinite rich in magnetite CO17, microtextural relationships indicate garnet crystallization contemporaneous to diopside (which commonly encloses garnet relics), magnetite, calcite and serpentine. Table 5 shows andradite compositions in both samples. Recasting analyses into end-member components (following Locock, 2008) gives ~ 98 mol% andradite in CO14 and ~ 95 mol% andradite in CO17. In CO14, Ca (3.011 apfu) is the only cation present at the dodecahedral site. The small amounts of Mg and Mn may be assigned to the octahedral site, in addition to $Fe^{3+}$ and to Al. Determination of the cell edge by means of XRPD analysis gives 12.0579(2) Å, nearly identical to the value of pure andradite (12.058(1) Å; Novak & Gibbs, 1971). The micro-Raman analyses do not show evidence of structural OH within CO14 garnet. In sample CO17, the common presence of garnet + serpentine intergrowths renders garnet analyses difficult (Fig. S3b). However, reliable analyses were possible on garnet filling magnetite

Table 4. Average microprobe compositions of serpentine minerals in pseudomorphic serpentinite CO15, rodingitic serpentinite CO14, and serpentinites rich in magnetite (CO17, CO18, CO24). Number in parentheses refers to standard deviation.

| | CO15 | | | CO14 | | CO17 | | CO18 | CO24 | |
|---|---|---|---|---|---|---|---|---|---|---|
| | 1 in mesh texture | 2 neoblast | 3* in bastite | 4** | 5 | 6 | 7 | 8 | 9 | 10* |
| | | | | lam. | prism. | lam. | prism. | prism. | h. refl. | l. refl. |
| wt.% | av. (11) | av. (11) | av.(5) | | av.(4) | av. (6) | av. (5) | av. (5) | av. (9) | av.(2) |
| MgO | 40.29 (46) | 40.58 (98) | 42.25 (24) | 40.65 | 40.77 (60) | 39.97 (23) | 40.25 (31) | 40.69 (28) | 41.38 (65) | 43.54 (20) |
| $Al_2O_3$ | 2.07 (37) | 0.63 (13) | 0.08 (5) | 2.29 | 0.76 (41) | 2.06 (38) | 1.10 (34) | 1.02 (19) | 0.60 (22) | 0.02 (3) |
| $SiO_2$ | 41.50 (49) | 44.67 (95) | 41.61 (31) | 42.67 | 43.95 (32) | 42.95 (37) | 43.77 (25) | 44.20 (23) | 44.52 (57) | 41.86 (40) |
| CaO | b.d.l. | b.d.l. | b.d.l. | b.d.l. | 0.27 (44) | 0.06 (2) | b.d.l. | b.d.l. | b.d.l. | b.d.l. |
| $Cr_2O_3$ | 0.28 (12) | 0.31 (15) | b.d.l. | b.d.l. | | b.d.l. | b.d.l. | b.d.l. | b.d.l. | b.d.l. |
| MnO | 0.08 (3) | 0.08 (3) | 0.16 (6) | 0.08 | 0.09 (2) | 0.10 (1) | 0.11 (1) | 0.12 (3) | 0.13 (12) | 0.20 (1) |
| FeO | 2.47 (32) | 1.55 (33) | 0.00 | 2.56 | 1.76 (32) | 3.37 (72) | 2.36 (17) | 2.51 (47) | 1.33 (30) | 0.00 |
| NiO | b.d.l. | b.d.l. | 0.09 (3) | b.d.l. | b.d.l. | b.d.l. | b.d.l. | b.d.l. | b.d.l. | b.d.l. |
| $Fe_2O_3$ | | | 1.90 (14) | | | | | | | 1.41 (4) |
| Total | 86.71 | 87.82 | 86.10 | 88.24 | 87.61 | 88.52 | 87.58 | 88.54 | 87.97 | 86.90 |
| for 7 oxygens: | | | | | | | | | | |
| Mg | 2.818 (27) | 2.774 (70) | 2.962 (13) | 2.787 | 2.802 (28) | 2.742 (14) | 2.772 (18) | 2.774 (11) | 2.822 (45) | 3.004 (18) |
| Al | 0.114 (20) | 0.034 (7) | 0.005 (2) | 0.124 | 0.041 (22) | 0.112 (20) | 0.060 (18) | 0.055 (10) | 0.032 (12) | 0.001 (1) |
| Si | 1.947 (14) | 2.048 (32) | 1.957 (12) | 1.963 | 2.026 (10) | 1.977 (20) | 2.022 (9) | 2.021 (9) | 2.037 (24) | 1.938 (16) |
| Ca | | | | | 0.013 (22) | 0.003 (1) | | | | |
| Cr | 0.010 (4) | 0.011 (5) | | | | | | | | |
| Mn | 0.003 (1) | 0.003 (1) | 0.006 (2) | 0.003 | 0.004 (1) | 0.004 (0) | 0.004 (0) | 0.004 (1) | 0.005 (5) | 0.008 (1) |
| $Fe^{2+}$ | 0.097 (13) | 0.059 (13) | 0.000 | 0.098 | 0.068 (13) | 0.130 (28) | 0.091 (6) | 0.096 (18) | 0.051 (11) | 0.000 |
| Ni | | | 0.003 (1) | | | | | | | |
| $Fe^{3+}$ | | | 0.067 (5) | | | | | | | 0.049 (1) |
| Sum | 4.990 | 4.929 | 5.000 | 4.975 | 4.953 | 4.967 | 4.948 | 4.951 | 4.947 | 5.000 |
| Mg/Si | 1.447 | 1.355 | 1.514 | 1.420 | 1.383 | 1.387 | 1.371 | 1.373 | 1.386 | 1.551 |

b.d.l. below detection limit (besides $TiO_2$, ZnO); * $Fe^{3+}$ calculated on base of stoichiometry after Droop (1987); ** single spot analysis; lam., lamellar; prism., prismatic; h. refl., l. refl., higher and lower reflectancy, respectively.

Table 5. Average microprobe compositions of silicates in rodingitic serpentinite CO14 and serpentinites rich in magnetite (CO17, CO18, CO24), and of brucite in CO24.

| | garnet | | | pyroxene | | | chlorite | | | | Olivine | Brucite |
|---|---|---|---|---|---|---|---|---|---|---|---|---|
| | CO14 | CO17 | CO17 | CO14 | CO17 | CO18 | CO14 | | CO18 | CO24 | CO24 | CO24 |
| wt.% | av. (10) | av. (5) | av. (5)* | av. (2) | av. (8) | av. (2) | ** | av. (3) | av. (5) | av.(8) | av. (4) | av. (5) |
| MgO | 0.08 (4) | 0.56 (14) | 0.56 | 18.43 (33) | 17.27 (36) | 18.05 (46) | 28.25 | 34.67 (6) | 34.44 (17) | 35.32 (80) | 55.49 (26) | 75.17 (1.81) |
| $Al_2O_3$ | 0.24 (21) | 0.58 (19) | 0.58 | 0.06 (3) | 0.08 (6) | 0.25 (36) | 22.56 | 15.99 (44) | 15.98 (19) | 15.55 (1.54) | b.d.l. | 0.18 (13) |
| $SiO_2$ | 35.18 (28) | 34.13 (42) | 34.13 | 54.76 (30) | 54.37 (37) | 55.20 (42) | 29.72 | 33.15 (34) | 33.27 (24) | 33.75 (88) | 42.49 (7) | b.d.l. |
| CaO | 33.15 (26) | 32.90 (60) | 32.90 | 26.29 (16) | 25.81 (22) | 25.99 (18) | 0.12 | 0.16 (16) | b.d.l. | b.d.l. | b.d.l. | b.d.l. |
| $TiO_2$ | 0.08 (3) | 0.25 (43) | 0.25 | b.d.l. | b.d.l. | b.d.l. | b.d.l. | b.d.l. | b.d.l. | b.d.l. | b.d.l. | b.d.l. |
| MnO | 0.15 (4) | 0.05 (2) | 0.05 | 0.07 (2) | 0.10 (5) | 0.13 (11) | 0.08 | 0.06 (3) | 0.04 (2) | 0.12 (3) | 0.88 (7) | 0.39 (6) |
| FeO | | | | 0.59 (38) | 2.47 (59) | 1.19 (66) | 8.32 | 2.76 (20) | 3.11 (17) | 3.50 (59) | 2.45 (21) | 2.54 (18) |
| $Fe_2O_3$ | 30.91 (41) | 31.29 (61) | 31.29 | | | | | | | | | |
| $H_2O$ | | | 1.00 | | | | | | | | | |
| Total | 99.80 | 99.78 | 100.78 | 100.20 | 100.10 | 100.83 | 89.06 | 86.79 | 86.85 | 88.24 | 101.31 | 78.27 |
| for 12 oxygens | | | * | for 6 oxygens | | | for 28 oxygens | | | | for 4 oxygens | for 3 oxygens |
| Mg | 0.010 (5) | 0.071 (18) | 0.069 | 0.994 (8) | 0.940 (18) | 0.968 (21) | 7.935 | 9.728 (30) | 9.664 (20) | 9.784 (191) | 1.941 (6) | 2.928 (11) |
| Al | 0.024 (21) | 0.058 (19) | 0.057 | 0.003 (1) | 0.004 (3) | 0.011 (15) | 5.011 | 3.547 (94) | 3.545 (48) | 3.407 (336) | b.d.l. | 0.005 (4) |
| Si | 2.982 (17) | 2.902 (16) | 2.834 | 1.981 (8) | 1.984 (7) | 1.986 (8) | 5.600 | 6.238 (64) | 6.261 (37) | 6.272 (174) | 0.997 (1) | b.d.l. |
| Ca | 3.011 (17) | 2.997 (32) | 2.927 | 1.019 (3) | 1.009 (8) | 1.002 (3) | 0.025 | 0.032 (33) | | | | |
| Ti | 0.005 (2) | 0.016 (27) | 0.016 | | | | | | | | | |
| Mn | 0.011 (3) | 0.003 (2) | 0.003 | 0.002 (1) | 0.003 (1) | 0.004 (3) | 0.012 | 0.009 (5) | 0.007 (3) | 0.018 (4) | 0.017 (1) | 0.009 (1) |
| $Fe^{2+}$ | | | | 0.018 (11) | 0.075 (18) | 0.036 (20) | 1.312 | 0.435 (32) | 0.490 (26) | 0.544 (91) | 0.048 (4) | 0.056 (5) |
| $Fe^{3+}$ | 1.972 (24) | 2.003 (54) | 1.955 | | | | | | | | | |
| $H_4^{4+}$ | | | 0.138 | | | | | | | | | |
| Sum | 8.016 | 8.051 | 8.000 | 4.017 | 4.014 | 4.007 | 19.895 | 19.988 | 19.966 | 20.025 | 3.003 | 2.997 |

b.d.l. below detection limits, besides: $Na_2O$, $K_2O$, $Cr_2O_3$ (garnet and pyroxene), $Na_2O$, $K_2O$, $Cr_2O_3$, NiO, ZnO (chlorite), $Cr_2O_3$, NiO, ZnO (olivine and brucite).
* recalculated with 1 wt% $H_2O$ for 8 cations and 12 oxygens (Locock, 2008) (see text). ** single spot analysis.
Number in parentheses refers to standard deviation.

fractures. Small amounts of Ti (0.016 apfu) are present. Its remarkable standard deviation (Table 5) points to a non homogeneous distribution, as already reported by Basso *et al.* (1984) in hydrogarnets from the Voltri massif and by Müntener & Hermann (1994) in a titanian andradite from the Malenco ultramafics. In CO17 garnet, there are, however, some other aspects to be investigated in more detail: even considering all iron as ferric, a remarkable surplus of cations (8.051 cations for 12 oxygens; Table 5) remains. Moreover, Si deficiency is significant; even allocating the total Al to the tetrahedral site, the (Si + Al) sum does not give 3 apfu. If analyses are recalculated according to Locock (2008), $Fe^{3+}$ is used to fill the remainder of the tetrahedral sites. Additionally, the oxide total is sometimes $\sim$ 1 % lower than 100 % (see Table S6), suggesting the presence of additional elements not detectable by microprobe (*e.g.,* hydrogen at the tetrahedral site). For this reason, a micro-Raman analysis was performed on the same grains used in the chemical analysis. The presence of structural OH in CO17 garnet is clearly shown by the occurrence of a small, but distinct, vibration peak at *ca.* 3540 $cm^{-1}$, coupled with a lower-intensity peak at 3610 $cm^{-1}$ (Fig. S6). These are very close to the value of 3545 $cm^{-1}$ obtained with Raman spectroscopy for hydroschorlomite in hydrothermally altered basalt (Hole 1256D, ODP Leg 206: Laverne *et al.*, 2006). Moreover, they closely match the value of 3555 $cm^{-1}$ for (hydrous) andradites in serpentinites obtained by infrared spectroscopy (Amthauer & Rossman, 1998). The very low intensity of the OH vibration peaks suggests a low $H_2O$ content in this andradite. Recalculation of the hydrous formula (Locock, 2008), with a rather low $H_2O$ content (tentatively, 1 % $H_2O$) improves charge balance with respect to the anhydrous analysis (Table 5); a small deficit of oxygens persists on the basis of 8 cations, which points to the presence of only ferric iron. Small amounts of Al are still needed to fill the remainder of the tetrahedral site because (Si + $H_4$) $<$ 3 apfu; $Fe^{3+}$ (1.955 apfu) is dominant in the octahedral site; the remainder of this site is filled by small amounts of Al and Ti. The dodecahedral site is not completely occupied by Ca (2.927 apfu), so the small amounts of Mg present may be assigned to this site. Andradite and hydroandradite are not uncommon in a number of serpentinite parageneses (Basso *et al.*, 1984; Frost & Beard, 2007 and references therein). From the same locality as specimen CO17 (Larsinaz), an andradite sample (94.1 mol% andradite, analysis reported also in Deer *et al.*, 1997), was collected and described by Sanero (1935) as a ''honey-yellow topazolite encrusting serpentinite''.

*Pyroxene*. In the rodingitic serpentinite CO14 and in the magnetite-rich serpentinites CO17 and CO18, clinopyroxene diopside occurs. It crystallizes in the serpentine matrix as mm-sized euhedral prisms (Fig. 3b). The composition of diopside is very homogeneous (Tables 5 and S7). In sample CO14, diopside is close to the end-member composition ($\sim$ 0.02 Fe apfu). In CO17 and CO18, the Fe contents are slightly higher ($\sim$ 0.08 and $\sim$ 0.04 apfu, respectively).

*Chlorite*. Chlorite is present in rodingitic serpentinite CO14 and in magnetite-rich serpentinites (*i.e.*, CO18 and CO24 samples), with a clinochlore composition (Table 5 and Fig. S7), characterized by small amounts of $Fe^{2+}$ ($\sim$ 0.5 apfu) and Mn substituting Mg ($\sim$ 10 apfu). Chlorite grown with calcite in sample CO14 has more Al ($\sim$ 5.0 apfu), trending towards amesite (Table 5, first column; Fig. S7), and is also richer in Fe (1.3 apfu). Notably, in sample CO24, chlorite enclosed in magnetite probably contains small amounts of $Fe^{3+}$, as suggested by the total cation sum exceeding 20 apfu (Tables 5 and S8).

*Olivine*. Olivine is present in the magnetite-rich serpentinite (CO24 sample) as μm-scaled grains dispersed in the serpentine matrix, associated with brucite and chlorite. This olivine is a nearly pure forsterite ($\sim$ 98 mol.%), with minor Mn content ($\sim$ 0.02 apfu), lacking Ni, Cr and Ti (Tables 5 and S9).

*Brucite.* Euhedral sub-mm-scaled grains of brucite were recognized in magnetite-rich serpentinite CO24, enclosed in magnetite, as coarse-grained flakes within pressure shadows around magnetite and also as very fine-grained intergrowths with lizardite. Brucite shows a typical micro-Raman spectrum characterized by strong peaks at 444 $cm^{-1}$ and 3651 $cm^{-1}$ (Fig. 7d). Brucite composition is reported in Tables 5 and S9. It contains small amounts of Fe ($\sim$ 0.06 apfu) and very small amounts ($\sim$ 0.01 apfu) of Mn and Al.

*Sulphides*. Pentlandite $(Ni,Fe)_9S_8$, heazlewoodite $Ni_3S_2$, millerite NiS and/or godlevskite $Ni_9S_8$ and pyrite occur in pseudomorphic serpentinite CO15 (Table 6). Chromian magnetite can grow together with pentlandite in submillimetric assemblages in the serpentine matrix. Pentlandite and heazlewoodite intergrowths can be present as alternating sub-micrometric lamellae ($<$10 μm, Fig. S2c); other assemblages such as pentlandite–millerite and/or godlevskite–heazlewoodite have been recognized by means of electron-microprobe analysis, although their intimate association can commonly give rise to overlapping analyses (Fig. S8). According to Misra & Fleet (1973), the Ni-Fe contents of natural pentlandite vary systematically with the type of assemblage; in CO15 pentlandite, the Ni quantity is in agreement with that found in the assemblages: (1) Pn–Hzl; (2) Pn–Py; (3) Py–Ml (–Vl), all sulphides present in sample CO15. Pentlandite, the most common sulphide, contains on average $\sim$ 28 at.% of Ni and $\sim$ 23 at.% of Fe (Co $\sim$ 2 at.%). Heazlewoodite is Co-free (Fe $\sim$ 2 at.%; Table 6). Pyrite is rarely detected. No native metals or alloys were recognized, in contrast to the serpentinized ultramafics of Mt. Avic (Diella *et al.*, 1994) and Balangero (Rossetti & Zucchetti, 1988a and b).

*Graphite*. In sample CO18, micro-Raman analyses carried out on elongated opaque inclusions in diopside, up to 10 μm long and parallel to the cleavage (Fig. 8), revealed a

Table 6. Average microprobe compositions of pentlandite (Pn) and heazlewoodite (Hzl) in pseudomorphic serpentinite CO15.

| | Pn | Hzl |
|---|---|---|
| wt.% | av. (53) | av. (4) |
| S | 32.78 (17) | 26.85 (20) |
| Fe | 27.35 (35) | 2.21 (68) |
| Co | 2.19 (17) | 0.08 (10) |
| Ni | 36.07 (19) | 71.68 (85) |
| Cu | 0.01 (1) | 0.00 (0) |
| Zn | 0.03 (5) | 0.04 (3) |
| As | 0.00 (0) | 0.01 (2) |
| Ag | 0.02 (1) | 0.03 (3) |
| Pb | 0.04 (2) | 0.06 (7) |
| Total | 98.48 | 100.96 |
| at.% | | |
| S | 47.23 (12) | 39.87 (30) |
| Fe | 22.62 (24) | 1.88 (58) |
| Co | 1.72 (14) | 0.07 (8) |
| Ni | 28.38 (14) | 58.12 (66) |
| Cu | 0.01 (1) | 0.00 (0) |
| Zn | 0.02 (4) | 0.03 (2) |
| As | 0.00 (0) | 0.01 (1) |
| Ag | 0.01 (1) | 0.01 (1) |
| Pb | 0.01 (1) | 0.01 (2) |

Number in parentheses refers to standard deviation.

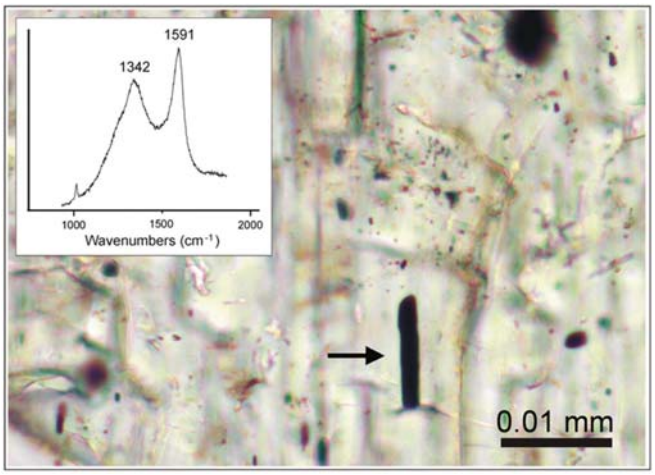


Fig. 8. Inclusion of graphitic material (black, oriented, elongated crystal) in diopside from serpentinite rich in magnetite (CO18). The inset shows the micro-Raman spectrum, indicating to partially disordered graphite as suggested by the D1 defect band at 1342 $cm^{-1}$ (Beyssac *et al.*, 2002 and references therein). The black, rounded inclusions are magnetite crystals; some very small, strongly elongated solid inclusions occur parallel to the graphite crystal and did not yield a Raman spectrum, probably because of their very fine-grained size. (online version in colour)

stronger band at 1591 $cm^{-1}$, and a second, broader and less intense band at *ca.* 1342 $cm^{-1}$. According to Beyssac *et al.* (2002), these inclusions are identified as partially disordered graphite.

## Discussion

### Magnetite, serpentinite and the seafloor

Magnetite mineralizations in orogenic serpentinite appear to be relatively scarce (*e.g.*, Singh & Srivastava, 1980; Gahlan *et al.*, 2006). Although magnetite is a typical product of serpentinization, it rarely occurs to give economic concentrations and Cogne represents so far, in terms of grade and tonnage, a unique deposit worldwide (Routhier, 1963). This suggests that formation of economic-grade magnetite deposits within serpentinite requires particular conditions. Compagnoni *et al.* (1981), based on the recognition of a primary stratigraphic cover on the Cogne serpentinite, suggested an oceanic origin of the magnetite concentration. A relationship with an ocean-floor setting is now further supported by recent findings in modern serpentinite-hosted hydrothermal systems. Hydrothermal deposits hosted in serpentinized peridotite and gabbro at the Lost City vent site (Mid-Atlantic Ridge; Kelley *et al.*, 2001, 2005) are directly akin to deposits reported from Alpine ophiolites. However, magnetite is only a trace-to-rare mineral in present-day marine metalliferous deposits (Li & Schoonmaker, 2003), although magnetic anomalies observed at slow and intermediate spreading ridges seem to confirm the presence of abundant magnetic minerals (Dyment *et al.*, 1997; Klein *et al.*, 2014). A number of serpentinization reactions, proposed to describe the formation of magnetite through alteration of the peridotite Fe-bearing silicates, can produce magnetite at low $T$ (50–300°C; *e.g.*, Evans, 2011). Because of the mineral abundance in peridotite, olivine hydration is the principal process that generates serpentine and magnetite through reactions such as

(1) olivine + $H_2O$ = serpentine + magnetite + $H_2$ (Mével, 2003);
(2) olivine + $H_2O$ = lizardite + magnetite + brucite + $H_2$ (McCollom & Bach, 2009);
(3) olivine + $H_2O$ + $O_2$ = serpentine + brucite + magnetite (Frost, 1985; Frost & Beard, 2007).

In these reactions, the ferrous iron contained in olivine as a fayalite component is partially oxidized to ferric iron, forming magnetite. The serpentinization can involve also orthopyroxene (*e.g.*, Frost & Beard, 2007). In this case, the formation of magnetite requires the oxidation of the ferrosilite component; taking into account the end-members forsterite, ferrosilite, serpentine, and magnetite, the reaction can be balanced as follows:

$$18\ Mg_2SiO_4 + 6\ FeSiO_3 + 24\ H_2O + 1\ O_2 = 12\ Mg_3Si_2O_5(OH)_4 + 2\ Fe_3O_4$$

### The mineralogical and petrological record from Cogne

Serpentinites from Cogne display heterogeneous bulk composition, trace-element content, mineralogical

assemblage and mineral chemistry. The investigated samples provide new constraints on the characteristics of this famous magnetite deposit, which allow speculation on the genesis of the ore.

The pseudomorphic serpentinite is the host rock of the magnetite ore. Magnetite (±Cr-bearing) occurs in relatively low amounts both in the serpentine pseudomorphs after olivine, in bastitic pseudomorphs after orthopyroxene and in the serpentine cross-cutting veins. Serpentine crystallized statically as lizardite and chrysotile, partially overgrown by antigorite. The occurrence of lizardite has never been reported previously in Cogne serpentinites. Lizardite and chrysotile are minerals found in low-*T* serpentinites, such as those exposed on the seafloor (Mével, 2003) or in ophiolite complexes not affected by metamorphism (*e.g.*, the serpentinites of Elba Island: Viti & Mellini, 1998). In the Central and Western Alps, lizardite occurs in serpentinites affected by low- and medium-*T* blueschist-facies metamorphism, *e.g.* Totalp (Peters, 1965); Queyras and Chenaillet (Schwartz *et al.*, 2013). The presence of antigorite replacing lizardite probably indicates a prograde formation. According to Schwartz *et al.* (2013), in the Western Alps, lizardite is progressively replaced by antigorite between 320 and 390°C, *i.e.*, with increasing *T*. In most serpentinites of the Western Alps, antigorite, associated with magnetite, is the typical serpentine phase stable during Alpine metamorphism (Compagnoni *et al.*, 1979, 1981; Groppo & Compagnoni, 2007; Fontana *et al.*, 2008; Debret *et al.*, 2013). The pseudomorphic serpentinite does not contain Cr-spinels or magnetite with Cr-rich cores, which have been instead observed in other Western-Alps deposits (*e.g.*, Mt. Avic; Diella *et al.*, 1994; Rossetti *et al.*, 2009). We show in Fig. 4 a previously unreported oscillatory zoning in magnetite, characterized by Cr-poor cores and Cr-rich inner euhedral rims with up to 17.0 wt.% $Cr_2O_3$. The outer rims appear partially resorbed and are characterized by *ca.* 2.0 wt.% $Cr_2O_3$. This zoning could be related to hydrothermalism, promoting dissolution-precipitation processes. We now propose that magnetite, as a product of *in situ* serpentinization, can be Cr-bearing. Chromium likely derives from the Cr-Tschermak component of the serpentinized orthopyroxene (cf. Cannat *et al.*, 1992; Miura *et al.*, 2011). Taking into account the end-members forsterite, ferrosilite, Cr-Tschermak, serpentine, and chromite, we balanced this possible reaction:

$$4\ Mg_2SiO_4 + 1\ FeSiO_3 + 1\ MgCr_2SiO_6 + 6\ H_2O = 3\ Mg_3Si_2O_5(OH)_4 + 1\ FeCr_2O_4$$

(It is interesting to note that, in pseudomorphic serpentinite, lizardite and antigorite do contain Cr (∼ 0.01 apfu).

According to the ODP and DSDP studies on the abyssal serpentinized peridotites, serpentinization should attain 60–70 % before magnetite formation peaks (Bach *et al.*, 2006). Moreover, a recent study of serpentinized peridotites recovered during the ODP shows that abundant magnetite (up to ∼ 6 wt.%) is formed at 200–300°C during serpentinization, whereas, at lower *T*, serpentinites are magnetite-poor (≤0.5 wt.%) and contain Fe-rich brucite instead (Klein *et al.*, 2014). The same study suggests that $H_2$ generation during serpentinization is not uniquely dependent on magnetite formation, but other sources of $H_2$ include the formation of ferric serpentine, (hydro-)andradite and iowaite. The relatively high magnetite content of the pseudomorphic serpentinite (*ca.* 4 vol.%) suggests that at Cogne, serpentinization occurred within the stability field of lizardite at *T* well above 200°C. Fe-Ni sulphides are associated to magnetite. These have been commonly observed in oceanic serpentinites (*e.g.*, Delacour *et al.*, 2008; Schwarzenbach *et al.*, 2012). The sulphur content measured in the pseudomorphic serpentinite of Cogne (718 ppm) is in the range of the oceanic (*e.g.*, 50–860 ppm, Alt & Shanks, 1998) and Ligurian serpentinites (Schwarzenbach *et al.*, 2012). The absence of alloys and the coexistence of pentlandite and heazlewoodite in the sample suggests that serpentinization occurred at moderate $fO_2$ - $fS_2$ conditions, in agreement with a complete degree of serpentinization (Frost, 1985). However, the association of magnetite with pyrrhotite, heazlewoodite, pentlandite, millerite and pyrite, is not an equilibrium assemblage. It implies strong variations in $fO_2$ (and $fS_2$) from relatively reducing (magnetite–heazlewoodite–pentlandite ± pyrrhotite) towards rather oxidizing (magnetite–millerite–pyrite) conditions (Frost, 1985; Schwarzenbach *et al.*, 2012). Serpentinization on the ocean floor may, in fact, occur at redox conditions that range from highly reducing to strongly oxidizing (Alt & Shanks, 1998; Schwarzenbach *et al.*, 2012). Based on the thermodynamic modelling of Frost (1985; Fig. 9), the opaque mineral assemblages allow the definition of the serpentinization conditions for Cogne in terms of oxygen fugacity (see also next section) and total sulphur species. The estimated values ($\log \Sigma S \approx -2$ to $-1$; $\log fO_2 \approx -36$ to $-30$) suggest a total serpentinization at intermediate to rather oxidizing redox conditions. These conditions differentiate the Cogne pseudomorphic serpentinite from Mt. Avic serpentinites, where Diella *et al.* (1994) described native metals (mainly Ni-Fe alloys) in equilibrium with magnetite and Fe and/or Ni sulphides (especially pyrrhotite, pentlandite and heazlewoodite). Similarly to Mt. Avic, Ni-Fe alloys, corresponding to strongly reducing conditions, were also reported in other metamorphic serpentinites from the Western Alps (Balangero; Lanzo; Sampeyre: Rossetti & Zucchetti, 1988a and b).

Compared to the pseudomorphic serpentinite, the bulk-rock compositions of rodingitic and magnetite-rich serpentinites show higher contents of Fe and lower amounts of Cr and volatiles (Table 2). These samples contain a higher amount of antigorite (but lizardite is often still recognizable), brucite and small olivine crystals characterized by a very high Mg content (Fo98). Silica and calcium are relevant in andradite-, diopside- and calcite-bearing samples, suggesting metasomatism sustained by $CO_2$-bearing

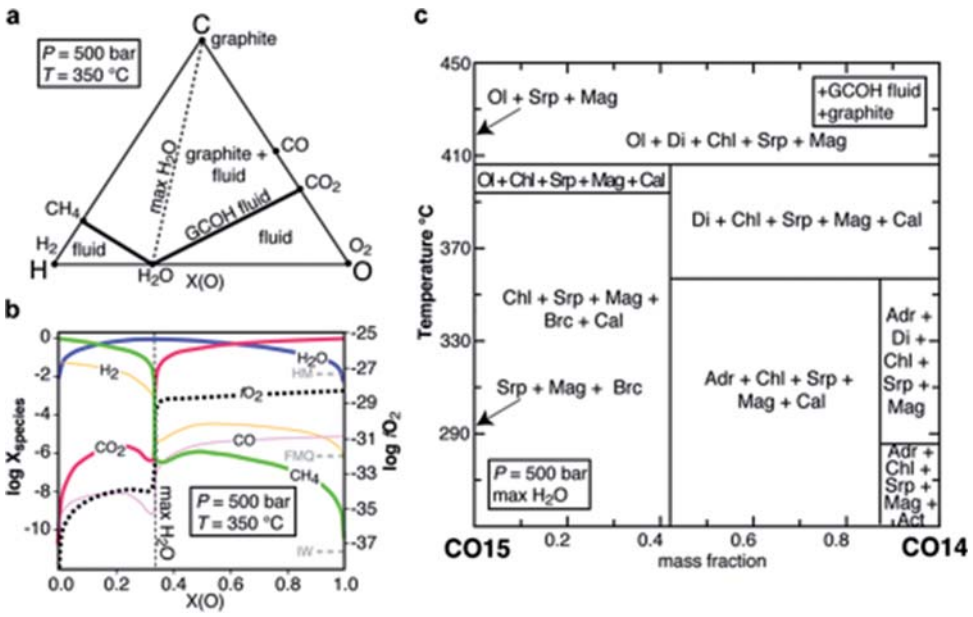


Fig. 9. Thermodynamic modelling of oceanic serpentinization and hydrothermal metasomatism. (a) Composition diagram for the C-O-H system at 500 bars and 350°C. Graphite-saturated fluids (GCOH fluid; *cf*. Connolly, 1995) plot on the thick black line. (b) Composition of GCOH fluids as a function of X(O) = [O/(O + H)]. Fluid speciation and oxygen fugacity are on the left and right vertical axes, respectively. Iron–wüstite (IW) and hematite–magnetite (HM) buffers are also shown for comparison. (c) Isobaric binary diagram for the system CFMAS + COH, where the composition of the system varies between the pseudomorphic serpentinite CO15 (left) and the rodingitic diopside + andradite rock CO14 (right). The fluid in equilibrium with the mineral assemblages is assumed to contain the maximum possible amount of $H_2O$ (see a, b and text for further details) For mineral abbreviations cf. Table 1; Act: actinolite. (online version in colour)

fluids. Graphite inclusions within diopside indicate carbon-saturation of the metasomatizing fluid.

## Thermodynamic modelling of serpentinites

The mineralogical associations found in the serpentinites of Cogne suggest oceanic serpentinization and metasomatic processes, which were probably mediated by fluids from hydrothermal vents on the Tethyian seafloor. Although it is impossible to directly access the chemical-physical conditions of such fluids, by analogy with data collected during oceanic surveys, we can assume a $T$ of $\sim$ 350°C and log $fO_2$ of $\sim$ –30 (*cf*. Tivey, 1995; Fig. 3). Vent fluids can contain variable amounts of carbon species, such as $CO_2$ and $CH_4$. The $CO_2$ content ranges from less than or equal to the total $CO_2$ levels present in seawater ($\sim$ 2.5 mmol/kg; $XCO_2$ [$=CO_2/(H_2O+ CO_2)$] = $4.5 \cdot 10^{-5}$; log $XCO_2 = -4.35$) to one order of magnitude more than seawater (German & Von Damm, 2003). The $CH_4$ and $H_2$ species, much less abundant than $CO_2$ in most hydrothermal systems, can be enriched only in ultramafic systems (German & Von Damm, 2003) where they are produced by serpentinization reactions (*e.g*., McCollom & Bach, 2009; see above). The occurrence of graphite in equilibrium with C-O-H fluids (*e.g*., Miura *et al.*, 2011) is of primary interest because, in this case, fluid composition and redox potential are strictly linked to each other. In graphite-saturated C-O-H fluids (GCOH fluids; Connolly, 1995), the redox potential fixes the fluid composition and *vice versa*. If the redox buffer capacity of rocks can be exhausted, as in the case of high fluid/rock ratios, the redox potential would be controlled externally by C-O-H fluids. The composition of the C-O-H fluid and therefore the redox conditions in force during the oceanic serpentinization and metasomatism recorded by the Cogne rocks can be deduced from the mineral assemblages observed, containing, in addition to magnetite (±Cr-bearing) and serpentine, carbonates (calcite), graphite, brucite, chlorite, diopside and almost pure andradite and hydroandradite garnet. In particular, andradite and hydroandradite garnet has been described in hydrothermal veins in oceanic massive serpentinites (*e.g*., Beard & Hopkinson, 2000; Frost & Beard, 2007; Ménez *et al.*, 2012). The low-temperature stability of andradite in C-O-H fluids has been investigated experimentally by Taylor & Liou (1978). Along the hematite-magnetite (HM) buffer, the authors suggested the following reaction:

$$\begin{aligned} &3\,SiO_2\,[\text{quartz}] + 3\,CaCO_3\,[\text{calcite}] \\ &\quad + 1/4\,Fe_2O_3\,[\text{hematite}] \\ &\quad + 1/2\,Fe_3O_4\,[\text{magnetite}] + 1/8O_2 \\ &\quad = Ca_3Fe_2Si_3O_{12}\,[\text{andradite}] + 3\,CO_2 \end{aligned} \qquad (1)$$

They demonstrated that the formation of andradite garnet at low temperature is favoured by low $XCO_2$ in the COH fluid and low pressures. At 500 bar, corresponding to 5000 m below sea level, andradite could form at 400°C with $XCO_2 \leq 0.1$ but the maximum possible $XCO_2$ diminishes asymptotically with decreasing temperature. The reaction of Eq. 1 can be applied only to quartz- and carbonate-

bearing rocks. Serpentinites do not contain quartz; therefore the following reaction could be envisaged in this case:

$$3/2\ Mg_3Si_2O_5(OH)_4\ [\text{lizardite}] + 3\ CaCO_3[\text{calcite}] + 2/3\ Fe_3O_4\ [\text{magnetite}] + 1/6\ O_2 + 3/2\ H_2O = 1\ Ca_3Fe_2Si_3O_{12}\ [\text{andradite}] + 9/2\ \ Mg(OH)_2\ [\text{brucite}] + 3\ CO_2 \quad (2)$$

To our knowledge, this reaction has not been investigated experimentally. The thermodynamic modelling of the reaction of Eq. 2 (Fig. S9) has been performed with the Perple_X computer package (http://www.perplex.ethz.ch; Connolly, 1990) and the database of Holland & Powell (1998), updated to 2004 (hp04ver.dat). As for Eq. 1, the formation of andradite at low $T$ is favoured by very low $XCO_2$ in the C-O-H fluid. At $T$ ranging from 250 to 400°C, the required log $XCO_2$ is –5 to –4, matching the $XCO_2$ of seawater (see above). Figure 9 (a,b) illustrates the thermodynamic modelling of a graphite-saturated C-O-H fluid (GCOH fluid) at 500 bar and 350°C. In natural rocks, graphite passes easily overlooked in petrographic observations, but it may occur as an accessory phase more frequently than previously believed. In the analysed samples of Cogne, we recognized graphite using Raman spectroscopy (sample CO18), so that we can assume that fluids involved were saturated in carbon. Since X(O) = [O/(O + H)], Figure 9b shows that fluids are nearly binary mixtures of $H_2O + CO_2$ for X(O)>1/3 and $H_2O + CH_4$ for X(O) < 1.3. At X(O) = 1/3, the content of water is maximum and the fluid is composed almost only of $H_2O$. All of the other species, including $CO_2$, are present in very minor amounts, from $10^{-3}$ to $10^{-6}$ molar fractions, comparable to the $XCO_2$ of seawater. Figure 9b also shows the $fO_2$ parameter varying in function of X(O) (dashed curve). Fluids with X(O) < 1/3 are ''reduced'', displaying low $fO_2$ values (log $fO_2$ < –34), while fluids with X(O) > 1/3 are ''oxidized'' with high $fO_2$ values (log $fO_2$ > –29). Fluids with maximum $H_2O$ content display a poorly defined log $fO_2$, broadly approaching the fayalite–magnetite–quartz (FMQ) buffer (log $fO_2$ = –32). This value agrees well with the estimates of Tivey (1995; Fig. 3) concerning the $fO_2$s of oceanic hydrothermal vents and with the sulphide paragenesis found in the Cogne rocks.

The constraints on the fluid composition allowed the construction of a binary phase diagram at 500 bar and 350°C, ranging from two representative bulk-rock compositions (Table 2): 1) pseudomorphic serpentinite CO15 and 2) rodingitic andradite-, diopside- and calcite-bearing rock CO14. At CO15, this $T-X$ diagram represents a model for the serpentinization of a peridotite in the pure FMS + COH system. The former peridotite undergoes hydration, becoming a magnetite ± brucite-bearing serpentinite. In fact, brucite has been observed in serpentinite CO24 associated to olivine (Fo98) neoblasts. According to Fig. 9c, prograde forsterite is expected to grow at the expense of brucite and lizardite above ~ 400°C. Towards rodingitic serpentinite, the diagram is a model for increasing contents of Ca, Fe and Al. Below 400°C, and for low degrees of metasomatism, the expected association should contain clinochlore and calcite in addition to lizardite, magnetite and brucite. Higher degrees of metasomatism will stabilize andradite at $T$ < 360°C and diopside at $T$ > 360°C in brucite-free rocks. Eventually, for compositions close to CO14, andradite and diopside coexist even at $T$ <360°C, and calcite becomes metastable. At $T$ < 300°C, diopside should be replaced by amphibole, never observed in the investigated samples.

Thermodynamic modelling suggests that mineral assemblages observed at Cogne match a process of seafloor serpentinization and Ca (±Al) metasomatism at 300–360°C conveyed by carbon-saturated C-O-H hydrothermal vent fluids characterized by $CO_2$ contents comparable to present-day seawater, capable of fixing the redox potential of rocks close to the FMQ buffer (Fig. 9b).

The same hydrothermal fluids probably mobilized the iron and concentrated magnetite. As shown by Gahlan *et al.* (2006), the existence of magnetite veins in serpentinite proves that hydrothermal fluids can efficiently act as carriers of iron. Considering the palaeoenvironmental setting (close to the ocean floor), iron was probably transported by the uprising heated sea waters as Cl complexes; complexation of iron with chloride ligands is indeed a major process affecting iron solubility in hydrothermal solutions (Wood & Samson, 1998). The distribution of Cr inside the magnetite grains of the pseudomorphic serpentinite (Fig. 4), which shows strong oscillatory zoning, may be explained by a process of selective leaching by hydrothermal fluids. Such a process involves an early formation of Cr-bearing magnetite (as a product of *in situ* serpentinization), followed by episodes of selective leaching of iron (and ''residual'' Cr enrichments) due to interaction with hydrothermal solution. Once brought to solution, the iron would have been redeposited – and concentrated – as magnetite, possibly as a consequence of the strong thermal and geochemical barrier of the ocean floor.

## Conclusions

Serpentinites from Cogne display heterogeneous bulk composition, trace-element content, mineralogical assemblage and mineral chemistry. The investigated samples provide new constraints on the characteristics of the biggest serpentinite-hosted magnetite ore deposit worldwide.

At Cogne, two types of magnetite are found: (i) Cr-bearing and (ii) Cr-free magnetite.

The former shows oscillatory zoning, with Cr-poor cores surrounded by Cr-rich rims (up to 17 wt.% $Cr_2O_3$). This magnetite shows compositions pertaining to inverse spinel structure (*i.e.*, magnetite). It is distinct from magnetite observed in other Western-Alps deposits characterized by Cr-rich cores (~ 45 wt.% $Cr_2O_3$) corresponding to normal spinel structure (*i.e.*, chromite). Cogne Cr-bearing magnetite is associated with lizardite, never having been reported previously in Cogne serpentinites, in a completely serpentinized peridotite due to low-temperature oceanic serpentinization, very weakly overprinted by Alpine metamorphism. We infer that Cr-bearing magnetite is produced by low-temperature

(200–300°C) serpentinization. Chromium probably derives from the Cr-Tschermak component of the serpentinized orthopyroxene.

The Cr-free magnetite, known as ''Cogne magnetite'', displays a nearly total inverse structure ($Fe^{2+}T = 0.07$ apfu) and is characterized only by a small $Fe^{2+} \leftrightarrow Mg$ substitution (2–15 mol% of magnesioferrite, $MgFe_2O_4$). The Cr-free magnetite occurs in serpentinites associated to antigorite (± lizardite), calcite and almost pure andradite/hydroandradite, ± diopside, ± chlorite, ± olivine and ± brucite, suggesting strong metasomatism sustained by $CO_2$-bearing fluids. The new finding of partially disordered graphite inclusions within diopside indicates carbon-saturation for the metasomatizing fluid.

The mineral assemblages observed at Cogne match a process of seafloor serpentinization and Ca (±Al) metasomatism at 300–360°C related to the circulation of carbon-saturated hydrothermal vent fluids characterized by $CO_2$ contents comparable to present-day seawater. The relict mineral assemblages, the crystal chemistry and geochemical data supported by thermodynamic modelling demonstrate the peculiarities of the Cogne ore deposit, suggesting that it may represent a Jurassic equivalent of modern serpentinite-hosted hydrothermal systems within an ocean-floor setting.

**Acknowledgements:** The authors are grateful to Prof. G. Pennacchioni for having donated the GP45 sample. Raul Carampin (CNR, IGG, Padova) and Andrea Risplendente (University of Milan) are thanked for their generous assistance with the microprobe analyses. Dr. F. Zorzi kindly performed XRPD analyses and cell edge determinations in garnets. S.C. would like to thank P. Frizzo for his help with opaque mineral identification and for useful suggestions. D. Brunelli is thanked for his advice on graphitic material. Helpful conversations with A. Della Giusta, G. Godard and C. Mével throughout the course of this work are gratefully acknowledged. The authors are particularly thankful to E.M. Schwarzenbach and J.C. Schumacher for critical reviews and helpful comments on an earlier version of the manuscript that was subsequently improved thanks to their help. Editorial handling by S. Conticelli is gratefully appreciated.

## References

Alt, J.C. & Shanks, W.C. (1998): Sulfur in serpentinized oceanic peridotites: serpentinization processes and microbial sulfate reduction. *J. Geophys. Res.*, **103**(B5), 9917–9929.

Amthauer, G. & Rossman, G.R. (1998): The hydrous component in andradite garnet. *Am. Mineral.*, **83**, 835–840.

Bach, W., Paulick, H., Garrido, C.J., Ildefonse, B., Meurer, W.P., Humphris, S.E. (2006): Unraveling the sequence of serpentinization reactions: petrography, mineral chemistry, and petrophysics of serpentinites from MAR 15°N (ODP Leg 209, Site 1274). *Geophys. Res. Lett.*, **33**, L13306.

Basso, R., Cimmino, F., Messiga, B. (1984): Crystal chemistry of hydrogarnets from three different microstructural sites of a basaltic metarodingite from the Voltri Massif (Western Liguria, Italy). *N. Jb. Miner. Abh.*, **148**(3), 246–258.

Beard, J.S. & Hopkinson, L. (2000): A fossil, serpentinization-related hydrothermal vent, Ocean Drilling Program Leg 173, Site 1068 (Iberia Abyssal Plain): some aspects of mineral and fluid chemistry. *J. Geophys. Res*, **105**(B7), 16,527–16,539.

Berndt, M.E., Allen, D.E., Seyfried, W.A. (2014): Reduction of $CO_2$ during serpentinization of olivine at 300°C and 500 bar. *Geology*, **24**, 351–354.

Bethaz, G. (1987): Le miniere di Cogne. *Rev. Valdotaine d'Hist. Natur.*, **41**, 149–154.

Beyssac, O., Rouzaud, J.-N., Goffé, B., Brunet, F., Chopin, C. (2002): Graphitization in a high-pressure, low-temperature metamorphic gradient: a Raman microspectroscopy and HRTEM study. *Contrib. Mineral. Petrol.*, **143**, 19–31.

Cannat, M., Bideau, D., Bougault, H. (1992): Serpentinized peridotites and gabbros in the Mid-Atlantic Ridge axial valley at 15°37'N and 16°52'N. *Earth Planet. Sci. Lett.*, **109**, 87–106.

Castello, P. (1981): Inventario delle mineralizzazioni a magnetite, ferro-rame e manganese del complesso piemontese dei calcescisti con pietre verdi in Valle d'Aosta. *Ofioliti*, **6**, 5–46.

Charlou, J.L., Fouquet, Y., Bougault, H., Donval, J.P., Etoubleau, J., Jean-Baptiste, P., Dapoigny, A., Appriou, P., Rona, P.A. (1998): Intense $CH_4$ plumes generated by serpentinization of ultramafic rocks at the intersection of the 15°20'N fracture zone and the Mid-Atlantic Ridge. *Geochim. Cosmochim. Acta*, **62**, 2323–2333.

Compagnoni, R., Elter, G., Fiora, L., Natale, P., Zucchetti, S. (1979): Nuove osservazioni sul giacimento di magnetite di Cogne in Valle d'Aosta. *Rend. Soc. Ital. Min. Petr.*, **35**, 755–766.

Compagnoni, R., Elter, G., Fiora, L., Natale, P., Zucchetti, S. (1981): Magnetite deposits in serpentinized lherzolites from the ophiolitic belt of the Western Alps, with special reference to the Cogne deposit (Aosta Valley). Proc. Intern. Symp. Mafic and Ultramafic Complexes, Athens, 9–11 October 1980, **3**, 376–394.

Connolly, J.A.D. (1990): Multivariable phase diagrams: an algorithm based on generalized thermodynamics. *Am. J. Sci.*, **290**, 666–718.

— (1995): Phase diagram methods for graphitic rocks and application to the system C-O-H-FeO-$TiO_2$-$SiO_2$. *Contrib. Mineral. Petrol.*, **119**, 94–116.

Dal Piaz, G.V., Gianotti, F., Monopoli, B., Pennacchioni, G., Tartarotti, P., Schiavo, A. (2010): Note illustrative della carta geologica d'Italia alla scala 1:50.000 Chatillon F. 91. Ispra-Servizio Geologico d'Italia, Treviso, 152 p.

Debret, B., Nicollet, C., Andreani, M., Schwartz, S., Godard, M. (2013): Three steps of serpentinization in an eclogitized oceanic serpentinization front (Lanzo Massif – Western Alps). *J. Metamorphic Geol.*, **31**, 165–186.

Deer, W.A., Howie, R.A., Zussman, J. (1997): Orthosilicates, Volume 1A, Rock-forming minerals, 2nd edition. The Geological Society, London, 919 p.

Delacour, A., Früh-Green, G.L., Bernasconi, S.M., Kelley, D.S. (2008): Sulfur in peridotites and gabbros at Lost City (30°N, MAR): Implications for hydrothermal alteration and microbial activity during serpentinization. *Geochim. Cosmochim. Acta*, **72**, 5090–5110.

Della Giusta, A., Carbonin, S., Russo, U. (2011): Chromite to magnetite transformation: compositional variations and cation distributions (southern Aosta Valley, Western Alps, Italy). *Per. Mineral.*, **80**(1), 1–17.

Di Colbertaldo, D., Di Furia, E., Rossi, F. (1967): Il giacimento a magnetite di Cogne in Val d'Aosta. *Istituto Lombardo*, **A101**, 361–394.

Diella, V., Ferrario, A., Rossetti, P. (1994): The magnetite ore deposits of the southern Aosta Valley: chromitite transformed during an Alpine metamorphic event. *Ofioliti*, **19**, 247–256.

Droop, G.T.R. (1987): A general equation for estimating $Fe^{3+}$ concentrations in ferromagnesian silicates and oxides from microprobe analyses, using stoichiometric criteria. *Mineral. Mag.*, **51**, 431–435.

Dyment, J., Arkani-Hamed, J., Ghods, A. (1997): Contribution of serpentinized ultramafics to marine magnetic anomalies at slow and intermediate spreading centres: insights from the shape of the anomalies. *Geophys. J. Int.*, **129**, 691–701.

Elter, G. (1971): Schistes lustrés et ophiolites de la zone piémontaise entre Orco et Doire Baltée (Alpes Graies). Hypothèses sur l'origine des ophiolites. *Géol. Alpine*, **47**, 147–169.

Evans, B.W. (2011): Lizardite versus antigorite serpentinite: magnetite, hydrogen, and life (?). *Geology*, **38**(10), 879–882.

Fontana, E., Panseri, M., Tartarotti, P. (2008): Oceanic relict textures in the Mount Avic serpentinites, Western Alps. *Ofioliti*, **33**(2), 105–118.

Frost, B.R. (1985): On the stability of sulfides, oxides, and native metals in serpentinite. *J. Petrol.*, **26**, 31–63.

Frost, B.R. & Beard, J.S. (2007): On silica activity and serpentinization. *J. Petrol.*, **48**(7), 1351–1368.

Gahlan, H.A., Arai, S., Ahmed, A.H., Ishida, Y., Abdel Aziz, Y.M., Rahimi, A. (2006): Origin of magnetite veins in serpentinite from the Late Proterozoic Bou-Azzer ophiolite, Anti-Atlas, Morocco: an implication for mobility of iron during serpentinization. *J. African Earth Sci.*, **46**, 318–330.

German, C.R. & Von Damm, K.L. (2003): Hydrothermal processes. *Treatise Geochem.*, **6**, 181–222.

Groppo, C. & Compagnoni, R. (2007): Metamorphic veins from the serpentinites of the Piemonte Zone, western Alps, Italy: a review. *Per. Mineral.*, **76**, 127–153.

Hafner, S. (1960): Metalloxide mit Spinellstruktur. *Schweiz. Mineral. Petrog. Mitt.*, **40**, 208–240.

Hill, R.J., Craig, J.R., Gibbs, G.V. (1979): Systematics of the spinel structure type. *Phys. Chem. Minerals*, **4**, 317–339.

Holland, T.J.B. & Powell, R. (1998): An internally consistent thermodynamic data set for phases of petrological interest. *J. Metamorphic Geol.*, **16**, 309–343.

Jervis, J. (1873): I tesori sotterranei d'Italia. Loescher, Torino, 92 p.

Jones, L.C., Rosenbauer, R., Goldsmith, J.I., Oze, C. (2010): Carbonate control of $H_2$ and $CH_4$ production in serpentinization systems at elevated P-Ts. *Geophys. Res. Lett.*, **37**, LI4306.

Kaczmarek, M.A. & Müntener, O. (2008): Juxtaposition of melt impregnation and high-temperature shear zones in the upper mantle; field and petrological constraints from the Lanzo peridotite (Northern Italy). *J. Petrol.*, **49**(12), 2187–2220.

Kelley, D.S. *et al*. (2005): A serpentinite-hosted ecosystem: the Lost City hydrothermal field. *Science*, **307**, 1428–1434.

Kelley, D.S., Karson, J.A., Blackman, D.K., Früh-Green, G.L., Butterfield, D.A., Lilley, M.D., Olson, E.J., Schrenk, M.O., Roe, K.K., Lebon, G.T., Rivizzigno, P., AT3-60 Shipboard Party. (2001): An off-axis hydrothermal vent field near the Mid-Atlantic Ridge at 30°N. *Nature*, **412**, 145–149.

Klein, F., Bach, W., Jöns, N., McCollom, T., Moskowitz, B., Berquó, T. (2009): Iron partitioning and hydrogen generation during serpentinization of abyssal peridotite from 15°N on the Mid-Atlantic Ridge. *Geochim. Cosmochim. Acta*, **73**, 6868–6893.

Klein, F., Bach, W., Humphris, S.E., Khal, W.-A., Jöns, N., Moskowitz, B., Berquò, T.S. (2014): Magnetite in seafloor serpentinite –Some like it hot. *Geology*, **42**, 135–138.

Laverne, C., Grauby, O., Alt, J.C., Bohn, M. (2006): Hydroschorlomite in altered basalts from Hole 1256D, ODP Leg 206: the transition from low-temperature to hydrothermal alteration. *Geochem. Geophys. Geosyst.*, **7**, 1–29. doi:10.1029/2005GC001180

Li, Y.-H. & Schoonmaker, J.E. (2003): Chemical Composition and Mineralogy of Marine Sediments. *Treatise Geochem.*, **7**, 1–35.

Locock, A.J. (2008): An Excel spreadsheet to recast analyses of garnet into end-member components, and a synopsis of the crystal chemistry of natural silicate garnets. *Comp. Geosci.*, **34**, 1769–1780.

Martin, S., Tumiati, S., Godard, G., Figaroli, M., Terrana, S. (2006): Il parco minerario della Valle d'Aosta. Report interno per ''Iron Route'' IIIB, Assessorato ambiente e territorio, Regione Valle d'Aosta.

Martin, S., Carbonin, S., Tumiati, S. (2009): First finding of Cr-rich magnetite from Liconi mine (Cogne) – Geological and mineralogical features. Abstract Volume, 9th Workshop on Alpine Geological Studies Cogne/Italy 16–18. September 2009.

McCollom, T.M. & Bach, W. (2009): Thermodynamic constraints on hydrogen generation during serpentinization of ultramafic rocks. *Geochim. Cosmochim. Acta*, **73**, 856–875.

Mellini, M. & Viti, C. (1994): Crystal structure of lizardite-1T from Elba, Italy. *Am. Mineral.*, **79**, 1194–1198.

Ménez, B., Pasini, V., Brunelli, D. (2012): Life in the hydrated suboceanic mantle. *Nature Geosci.*, **5**, 133–137.

Mével, C. (2003): Serpentinization of abyssal peridotites at mid-ocean ridges. *C. R. Geosciences*, **335**, 825–852.

Misra, K.C. & Fleet, M.E. (1973): The chemical compositions of synthetic and natural pentlandite assemblages. *Econ. Geol.*, **68**, 518–539.

Miura, M., Arai, S., Mizukami, T. (2011): Raman spectroscopy of hydrous inclusions in olivine and orthopyroxene in ophiolitic harzburgite: implications for elementary processes in serpentinization. *J. Miner. Petrol. Sci.*, **106**, 91–96.

Müntener, O. & Hermann, J. (1994): Titanian andradite in a metapyroxenite layer from the Malenco ultramafics (Italy): implications for Ti-mobility and low oxygen fugacity. *Contrib. Mineral. Petrol.*, **116**, 156–168.

Nadoll, P., Angerer, T., Mauk, J.L., French, D., Walshe, J. (2014): The Chemistry of hydrothermal magnetite: A review. *Ore Geol. Rev.*, **61**, 1–32. doi:10.1016/j.oregeorev.2013.12.013

Nakagiri, N., Manghnani, M.H., Ming, L.C., Kimura, S. (1986): Crystal structure of magnetite under pressure. *Phys. Chem. Minerals*, **13**, 238–244.

Novak, G.A. & Gibbs, G.V. (1971): The crystal chemistry of the silicate garnets. *Am. Mineral.*, **56**, 791–825.

Peters, Tj. (1965): A water-bearing andradite from the Totalp serpentine (Davos, Switzerland). *Am. Mineral.*, **50**, 1482–1486.

Rinaudo, C., Gastaldi, D., Belluso, E. (2003): Characterization of chrysotile, antigorite and lizardite by FT-Raman spectroscopy. *Can. Mineral.*, **41**, 883–890.

Rossetti, P. & Zucchetti, S. (1988a): Occurrence of native iron, Fe-Co and Ni-Fe alloys in the serpentinite from Balangero asbestos mine (Western Italian Alps). *Ofioliti*, **13**, 43–56.

Rossetti, P. & Zucchetti, S. (1988b): Early-alpine ore parageneses in the serpentinites from the Balangero asbestos mine and Lanzo massif (Internal Western Alps). *Rend. Soc. Ital. Min. Petr.*, **43**, 139–149.

Rossetti, P., Gatta, G.D., Diella, V., Carbonin, S., Della Giusta, A., Ferrario, A. (2009): The magnetite ore districts of the southern Aosta Valley (Western Alps, Italy): a mineralogical study of metasomatized chromite ore. *Mineral. Mag.*, **73**(5), 737–751.

Routhier, P. (1963): Les gisements métallifères: géologie et principes de recherche. Masson éd, Paris, 1282 p.

Rozenson, I., Bauminger, E.R., Heller-Kallai, L. (1979): Mössbauer spectra of iron in 1:1 phyllosilicates. *Am. Mineral.*, **64**, 893–901.

Sanero, E. (1935): Sopra due granati delle miniere di Cogne in Val d'Aosta. *Per. Mineral.*, **6**, 213–220.

Schwartz, S., Guillot, S., Reynard, B., Lafay, R., Debret, B., Nicollet, C., Lanari, P., Auzende, A.L. (2013): Pressure–temperature estimates of the lizardite/antigorite transition in high pressure serpentinites. *Lithos*, **178**, 197–210.

Schwarzenbach, E.M., Früh-Green, G.L., Bernasconi, S.M., Alt, J.C., Shanks, W.C., Gaggero, L., Crispini, L. (2012): Sulfur geochemistry of peridotite-hosted hydrothermal systems: comparing the Ligurian ophiolites with oceanic serpentinites. *Geochim. Cosmochim. Acta*, **91**, 283–305.

Singh, R.N. & Srivastava, S.N.P. (1980): Ophiolites and associated mineralizations in the Naga Hills, north-eastern India. *in* ''Ophiolites-Procedings. International Ophiolite Symposium Cyprus 1979'', A. Panayiotou, ed. Cyprus Geological Survey, Nicosia, 758–764.

Stella, A. (1921): Le miniere di ferro d'Italia. Lattes, Torino, 426 p.

Taylor, B.E. & Liou, J.G. (1978): The low-temperature stability of andradite in C-O-H fluids. *Am. Mineral.*, **63**, 378–393.

Tivey, M.K. (1995): Modeling chimney growth and associated fluid flow at seafloor hydrothermal vent sites. *AGU Geophys. Monogr.*, **91**, 158–177.

Toft, P.B., Arkani-Hamed, J., Haggerty, S.E. (1990): The effects of serpentinization on density and magnetic susceptibility: a petrophysical model. *Phys. Earth Planet. Inter.*, **65**, 137–157.

Verwey, E.J.W. & de Boer, J.H. (1936): Cation arrangement in a few oxides with crystal structures of the spinel type. *Rec. Trav. Chim. Pays-Bas*, **55**(6), 531–540.

Viti, C. & Mellini, M. (1998): Mesh textures and bastites in the Elba retrograde serpentinites. *Eur. J. Mineral.*, **10**, 1341–1359.

Whitney, D.L. & Evans, B.W. (2010): Abbreviations for names of rock-forming minerals. *Am. Mineral.*, **95**, 185–187.

Wicks, F.J. & O'Hanley, D.S. (1988): Serpentine minerals: structures and petrology. *in* ''Hydrous Phyllosilicates'', S.W. Bailey, ed. *Rev. Mineral.*, **19**, 91–167.

Wood, S.A. & Samson, I.M. (1998): Solubility of ore minerals and complexation of ore metals in hydrothermal solutions. *in* ''Techniques in hydrothermal ore deposits geology'', J.P. Richards & P.B. Larson, eds. *Rev. Econ. Geol.*, **10**, 33–80.

Zucchetti, S., Mastrangelo, F., Rossetti, P., Sandrone, R. (1988): Serpentinization and metamorphism: their relationships with metallogeny in some ophiolitic ultramafics from the Alps. *in* ''Zuffar' Days Symposium in Honor of Piero Zuffardi'', University of Cagliari, Cagliari, October 10–15, 1988, 137–159.

*Received 1 April 2014*
*Modified version received 3 September 2014*
*Accepted 22 September 2014*